

UCSF

UC San Francisco Previously Published Works

Title

MYC phase separation selectively modulates the transcriptome.

Permalink

<https://escholarship.org/uc/item/5k57280t>

Journal

Nature Structural & Molecular Biology, 31(10)

Authors

Yang, Junjiao

Chung, Chan-I

Koach, Jessica

et al.

Publication Date

2024-10-01

DOI

10.1038/s41594-024-01322-6

Peer reviewed



Published in final edited form as:

Nat Struct Mol Biol. 2024 October ; 31(10): 1567–1579. doi:10.1038/s41594-024-01322-6.

MYC phase separation selectively modulates the transcriptome

Junjiao Yang^{1,2,3}, Chan-I Chung^{1,2,3}, Jessica Koach⁴, Hongjiang Liu⁵, Ambuja Navalkar⁶, Hao He^{1,2}, Zhimin Ma^{1,2}, Qian Zhao^{1,2}, Xiaoyu Yang⁵, Liang He^{1,2}, Tanja Mittag⁶, Yin Shen⁵, William A. Weiss⁴, Xiaokun Shu^{1,2,7,*}

¹Department of Pharmaceutical Chemistry, University of California, San Francisco, San Francisco, California, USA.

²Cardiovascular Research Institute, University of California, California, USA

³These authors contributed equally.

⁴Departments of Neurology, Neurological Surgery, Pediatrics, and Helen Diller Family Comprehensive Cancer Center, University of California, San Francisco, San Francisco, CA, USA.

⁵Institute for Human Genetics, Departments of Neurology, Weill Institute for Neurosciences, University of California, San Francisco, San Francisco, CA, USA.

⁶Department of Structural Biology, St. Jude Children's Research Hospital, 262 Danny Thomas Place, Memphis, TN 38105, USA.

⁷Helen Diller Family Comprehensive Center, University of California, California, USA

Abstract

Dysregulation and enhanced expression of *MYC* transcription factors (TFs) including *MYC* and *MYCN* contribute to the majority of human cancers. For example, *MYCN* is amplified up to several hundred-fold in high-risk neuroblastoma. The resulting overexpression of N-myc aberrantly activates genes that are not activated at low N-myc levels and drives cell proliferation. Whether increasing N-myc levels simply mediate binding to lower-affinity binding sites in the genome or fundamentally changes the activation process remains unclear. One such activation mechanism that could become important above threshold levels of N-myc is the formation of aberrant transcriptional condensates through phase separation. Phase separation has recently been linked to transcriptional regulation, but to which extent it contributes to gene activation remains an open question. Here we characterized the phase behavior of N-myc and showed that it can form dynamic condensates that have transcriptional hallmarks. We tested the role of phase separation in N-myc-regulated transcription by using a chemogenetic tool that allowed us to compare non-

*Correspondence to: Xiaokun Shu (xiaokun.shu@ucsf.edu).

Author contributions: X.S. conceived the project. J.Y., C-I.C. and L.H. made the constructs. J.Y. performed N-myc phase separation and colocalization with other proteins in cells. C-I.C. conducted imaging of small molecule-induced N-myc phase separation and analyzed colocalization with other proteins. C-I.C. performed and analyzed nascent RNA labeling, RT-qPCR and RNA-seq. J.Y., J.K., X.S. and W.A.W. planned and performed experiments to analyze expression of endogenous N-myc protein in the neuroblastoma cells. H.L. processed RNA-seq data. H.L., H. H., Z. M., C-I.C, J.Y., Q.Z., X.Y., X.S., Y.S. analyzed RNA-seq data. A.N. and T.M. designed and analyzed the in vitro experiments. A.N. conducted the in vitro experiments. J.Y., C-I.C, T.M., X.S. wrote the manuscript. All authors contributed to the final draft.

Competing interests: X.S. and W.A.W. are co-founders of Granule Therapeutics. The remaining authors declare no competing interests.

phase-separated and phase-separated conditions at equivalent N-myc levels, which both showed a strong impact on gene expression compared to no N-myc expression. Interestingly, we discovered that only a small percentage of <3% of N-myc-regulated genes is further modulated by phase separation, but that these events include the activation of key oncogenes and the repression of tumor suppressors. Indeed, phase separation increases cell proliferation, corroborating the biological effects of the transcriptional changes. However, our results also show that >97% of N-myc-regulated genes are not affected by N-myc phase separation, demonstrating that soluble complexes of TFs with the transcriptional machinery are sufficient to activate transcription.

Introduction

MYC family transcription factors are major contributors to human tumorigenesis. Expression of *Myc* is deregulated and enhanced in many types of cancers due to copy number changes, chromosomal translocations, or upstream oncogenic signaling^{3–6}. For instance, *MYCN* is highly amplified 100-to-300 fold in nearly half of high-risk neuroblastoma patients^{7–10}. While upregulated *Myc* expression induces tumor development in many tissues, depletion of *Myc* abolishes tumorigenesis and results in tumor regression in various tumor models^{11–15}. Given that high *Myc* expression does not only enhance the transcriptional activation but changes the pattern of gene expression to promote cell proliferation, one important question is how the changes to the transcriptional program are caused by rising *Myc* levels. Do increasing *Myc* concentrations allow binding to progressively lower-affinity binding sites in the genome¹⁶, or does the activation mechanism fundamentally change?

One potential mechanism for a fundamental change in the activation mechanism is the formation of transcriptional condensates through phase separation (PS). Phase separation mediates the formation of a dense phase above a threshold concentration of biomolecules^{17–21}. Recently, many transcription factors (TFs) have been reported to undergo PS and form biomolecular condensates (also known as membraneless compartments, granules, or liquid-like droplets) when protein concentration surpasses a threshold concentration^{22–26}. Biomolecular condensates compartmentalize interacting proteins and signaling complexes in percolated dense phases^{18–20,25,27–29}. Condensates of transcription factors have been proposed and demonstrated to recruit transcriptional machinery^{23,24,30}. Importantly, whether phase separation influences the transcriptional output in any way remains a matter of discussion³¹. Dissecting this role of phase separation is challenging. Mutations that modulate phase behavior are employed in many studies in order to understand the correlation between the underlying driving force for protein phase separation and function^{23,32}, but such mutations can also alter the ability of TFs to form soluble (and therefore diffuse) complexes with the transcriptional machinery^{22,33}. Such diffuse complexes form via transient multivalent interactions as characterized in detail for the yeast transcription factor *GCN4*³⁴. These same interactions are also conducive to mediating the formation of the three-dimensional network structure spanning condensates. Furthermore, associative biomolecules that drive phase separation are expected to form higher-order complexes or so-called pre-percolation clusters, below the saturation concentration^{35,36}. It thus remains an open question whether the transcriptional output observed in the presence of

transcriptional condensates would also be achieved without phase separation. Interestingly, a recent study proposed that phase separation does not enhance transcription³⁷. In this study, TF expression levels were changed to compare activity in cells with and without condensates near the threshold concentration of PS, but assigning the threshold level for the formation of condensates on chromatin was challenging. Furthermore, changing TF levels will itself influence activity. Given that aberrant transcriptional condensates may offer attractive opportunities to develop new therapeutics^{38–40}}, these challenges in understanding the transcriptional function of phase separation prompt us to design tools that allow us to examine transcriptional activity after turning on phase separation without modifying expression levels or making mutations.

Here, we apply a chemogenetic tool⁴¹ to turn on N-myc phase separation in a neuroblastoma cell line and compare transcriptional activity between cells with and without N-myc phase separation at equal N-myc levels. We discover that N-myc condensates are transcriptionally active and result in gene expression patterns that are highly similar to those with diffuse N-myc. However, the expression of a small percentage of genes is modulated upon phase separation, and these may be important for Myc-dependent oncogenesis. Therefore, our work reveals a functional role for phase separation of the dysregulated N-myc oncoprotein transcription factor in cancer, and at the same time it shows that phase-separation of N-myc does not promote transcription of all target genes.

RESULTS

N-myc undergoes phase separation in cells

To test whether N-myc forms condensates, we used immunofluorescence imaging in *MYCN*-amplified human Kelly neuroblastoma cells. Our imaging data indicated that N-myc protein formed puncta in the nucleus (Fig. 1a), which were not observed upon treatment with a MYC/MAX dimerization inhibitor that was previously shown to degrade Myc⁴² (Extended Data Fig. 1). Importantly, in *MYCN*-nonamplified SH-EP neuroblastoma cells, we did not observe obvious punctate structures (Fig. 1a), consistent with the western blot analysis showing no N-myc expression in SH-EP cells (Extended Data Fig. 2). To characterize the phase behavior of N-myc, we expressed the fusion protein N-myc-mEGFP in SH-EP cells that did not express N-myc and carried out live-cell imaging. N-myc-mEGFP was evenly distributed and did not form punctate structures until its expression level was above a saturation concentration (Fig. 1b).

Our quantitative analysis yielded the percentage of N-myc in punctate structures. The percentage is dependent on protein expression levels, and it was ~30 – 50% at a N-myc level of 500 nM. We estimated the concentration of N-myc protein in single cells based on purified mEGFP and were able to determine that the range (or confidence interval) of saturation concentrations of N-myc was ~ 300 – 400 nM (see Methods, Extended Data Fig. 3a and Supporting Fig. S1–2). Our data show an interval rather than a single threshold concentration, consistent with a previous report that in the cellular context, heterotypic phase separation results in non-fixed saturation concentrations⁴³. Below the range of saturation concentrations, e.g. at ~ 250 nM, N-myc was evenly distributed in the nucleus (Fig. 1b, upper-right). Above the saturation concentrations, e.g. at ~500 nM, N-myc formed puncta

in the nucleus (Fig. 1b, lower-right). Thus, our data show that N-myc-mEGFP undergoes a concentration-dependent spatial rearrangement consistent with phase separation. We estimated that the N-myc concentration is around $0.6 \mu\text{M}$ in the Kelly cells (Extended Data Fig. 3b–d). We characterized the connection of the number and size of the N-myc puncta with the protein levels and found that the number of N-myc puncta increases as the N-myc protein level increases (Extended Data Fig. 4a). The size of N-myc puncta is in the range of $0.4 - 1 \mu\text{m}$ (diameter), and this distribution is independent of the protein levels (Extended Data Fig. 4b). This suggests that N-myc tends to form additional puncta when the protein level increases.

Next, we determined whether the N-myc puncta exhibit fluid properties. We conducted time-lapse imaging of N-myc condensates. The puncta fused and coalesced rapidly and relaxed into a spherical shape (Fig. 1c). Quantitative analysis indicated that the aspect ratio of two coalescing puncta over time can be fitted to a single exponential curve (Fig. 1c, lower left), which is a wellknown characteristic of coalescing liquid droplets^{44,45}. We then calculated the inverse capillary velocity ($= \eta/\gamma$; here η is viscosity; γ is droplet's surface tension), which was 1.25 ± 0.42 (s/ μm) (Fig. 1c, lower right). Thus, the N-myc puncta are fluid condensates formed by phase separation when the concentration of N-myc-mEGFP exceeds threshold levels, which are reached by many *MYCN*-amplified cancer cell lines.

N-myc, which encompasses 464 residues, has an intrinsically disordered transactivation domain (TAD) (Fig. 1d)⁴⁶, which encompasses conserved N-terminal motifs including three "Myc boxes" (MB0-II) from residues 1 – 137 residues^{47,48}. To examine the role of the TAD in N-myc PS, we designed and characterized a TAD truncation mutant (N-myc¹³⁸⁻⁴⁶⁴). Live cell imaging revealed that this mEGFP-tagged fusion protein (N-myc¹³⁸⁻⁴⁶⁴-mEGFP) no longer formed condensates even above $2 \mu\text{M}$ concentration (Fig. 1d), ~ 5 -fold above the threshold concentration of PS for full-length N-myc. Therefore, our data demonstrate that N-myc PS requires the intrinsically disordered TAD, consistent with PS of many other proteins that also rely on their IDR¹⁹.

N-myc condensates contain MAX and genomic DNA

To determine whether the N-myc condensates are active in transcription, we examined whether they contain MAX, the DNA-binding and dimerization partner of N-myc. To image MAX in living cells, we tagged it with mKO3, a red fluorescent protein. Confocal fluorescence imaging revealed that MAX also had a punctate appearance, and that MAX and N-myc largely colocalized in the same puncta (Fig. 2a). In cells without N-myc-mEGFP, MAX did not have a punctate appearance (Supporting Fig. S3). These data suggest that N-myc condensates recruit its DNA-binding partner MAX or that N-myc and MAX co-condense.

To test whether N-myc condensates localized to DNA loci of an example N-myc target gene, we chose *TP53*^{49,50} and labeled the *TP53* DNA locus using fluorescence in situ hybridization (FISH). Confocal fluorescence imaging showed that some N-myc condensates were found at the genomic DNA locus of *TP53* (Fig. 2b).

N-myc condensates contain transcriptional markers

To further test whether N-myc condensates may be transcriptionally active, we determined whether they contained transcriptional machinery, including the Mediator and RNA polymerase II (Pol II). First, immunofluorescence imaging showed that the Mediator of RNA polymerase II transcription subunit 1 (MED1) had punctate localization in cells, which is consistent with a previous work⁵¹. Further, N-myc condensates contain MED1, but not all MED1 puncta overlap with N-myc (Fig. 2c). Second, we conducted immunofluorescence imaging for Pol II phosphorylated at Ser5 (Pol II S5p) in the C-terminal domain. Our results revealed punctate localization of Pol II S5p, which was colocalized with N-myc condensates (Fig. 2d). Together, our data show that N-myc-positive condensates contain components of the transcriptional machinery. N-myc condensates also contain nascent RNA (Fig. 2e, Methods). We further quantified colocalization of N-myc condensates with MAX, MED1, Pol II S5p and nascent RNAs (Fig. 2f, Methods). Lastly, we conducted immunofluorescence imaging of the endogenous N-myc in Kelly cells, which revealed that N-myc condensates colocalized with MAX, MED1, Pol II S5p and nascent RNA (Extended Data Fig. 5a–d), but not other TFs such as c-Jun (Extended Data Fig. 5e). Taken together, our data indicates that the exogenously expressed N-myc-mEGFP formed condensates that contain transcriptionally active machinery in SH-EP cells, which is similar to the endogenous N-myc condensates in Kelly cells.

Disassembly and assembly of N-myc condensates during mitosis

Condensates can coalesce, and the coalescence of transcriptional condensates may bring distant genomic elements into juxtaposition and impact gene transcription³³. Therefore, dynamic properties of condensates are expected to influence biological functions. Several biomolecular condensates have previously been shown to dissolve during mitosis⁵². Here we asked whether N-myc condensates also assembled and disassembled during mitosis. We used live-cell confocal imaging and observed that N-myc condensates disassembled upon mitotic entry (Fig. 3a, left panel). When cells enter mitosis, chromatin condenses even though nuclear chromatin is already compacted in the interphase. Many transcription factors dissociate from chromatin upon entry into mitosis^{53,54}. Hence, we investigated the temporal relationship between chromatin condensation upon entry into mitosis and N-myc condensate dissolution. To image and quantify the volume of chromatin, we tagged histone 2B (H2B) with mIFP, an infrared fluorescent protein^{55–57}. Time-lapse fluorescence imaging showed that the dissolution of N-myc condensates preceded chromatin condensation by ~ 6 minutes (Fig. 3a, right panel). The dissolution of N-myc condensates also occurred before the breakdown of the nuclear envelope (Fig. 3a, T ~ 18 min.). Because most transcription factors dissociate from chromatin during chromatin condensation when cells enter mitosis, one possible factor that contributes to the dissolution of N-myc condensates could be the loss of its binding to E-box DNA. This is a possible scenario given the biochemical data that E-box DNA binding contributes to N-myc phase separation (see next section).

We then determined whether N-myc condensates reformed upon mitotic exit. Indeed, our imaging data showed that N-myc condensates re-assembled. Chromatin de-condensation also occurred upon mitotic exit as reported in a previous study⁵⁷. Interestingly, during mitotic exit, N-myc condensates formed after chromatin decondensation with a delay of ~ 6

minutes (Fig. 3b). This mirrors mitotic entry, where the dissolution of N-myc condensates occurred before chromatin condensation. Because when cells exit mitosis, the chromatin decondenses and the previously dissociated transcription factors re-access their cognate DNA, formation of N-myc condensates upon mitotic exit is likely caused by re-association of N-myc with E-box sequences.

Overall, our experiments reveal dynamic regulation of N-myc condensates during the cell cycle, and this correlated with chromatin structural changes (condensation and decondensation). Because many transcription factors disengage from chromatin when cells enter mitosis and re-associate with chromatin when cells exit mitosis^{53,54}, we investigated a potential role of the N-myc DNA-binding domain bHLH-LZ (366–464 aa) on N-myc phase separation. We truncated bHLH-LZ and measured phase separation of this truncation mutant N-myc^{1–365}. Indeed, the range of saturation concentrations of this mutant is ~ 620 – 720 nM (Fig. 3c, blue box, Extended Data Fig. 6), which is ~ 2-fold more than that of full-length N-myc (~ 300 – 400 nM, Fig. 1b; red box in Fig. 3c). Our data thus suggest that the DNA-binding domain contributes to N-myc phase separation. We also found that MAX contributed to N-myc PS because knock-out of MAX increased the saturation concentration of N-myc. This effect can be rescued by re-expression of MAX (Extended Data Fig. 7a), but overexpression of MAX has little effect on the saturation concentration (Extended Data Fig. 7b).

E-box DNA enhances condensate formation of purified N-myc

Given that we found a contribution of the DNA-binding domain to N-myc condensate formation, we sought to understand quantitatively how phase separation of N-myc is modified by binding to different DNA sequences. We thus turned to experiments in vitro with purified proteins and defined DNA oligonucleotides. CD spectroscopy showed that recombinant N-myc had a partially helical secondary structure as expected⁵⁸ (Fig. 4a). N-myc/MAX bound to a DNA oligomer containing a single E-box (CACGTG in 26-mer, called 1Ebox DNA from hereon) (Fig. 4b). Phase separation of purified c-Myc-mEGFP (at a concentration of 12 μ M) was previously reported²³. Here we characterized the effect of DNA on phase separation of N-myc. N-myc/Max complexes (at 10 and 3 μ M, respectively) did not phase separate, but the addition of 1Ebox DNA into the N-myc/MAX solution promoted phase separation (Fig. 4c). 3Ebox and 7Ebox DNA (with 3 and 7 repeats of E-box sequences, respectively) promoted phase separation at lower concentrations. Similarly, DNA oligos with non-canonical E-box sequences with 1 or 7 repeats also promoted phase separation at similar concentrations as canonical E-box sequences (Extended Data Fig. 8). These effects were also observed using an analytical HPLC approach (Methods, Fig. 4d). On the other hand, the addition of non-Ebox DNA (of the same length as 7Ebox DNA), did not result in phase separation. E-box DNA in the absence of protein did not undergo phase separation (Fig. 4c). Together these results show that N-myc/MAX dimers phase separate, that interactions with E-box DNA enhance their phase separation, and that E-box DNA with multiple binding motifs can effectively scaffold N-myc/MAX phase separation in a pre-wetting transition (Fig. 4e), which has also been observed for other transcription factors⁵⁹.

Structural basis of transcriptional machinery recruitment

Because our data indicated that both the TAD and bHLH-LZ domains are important for N-myc PS, we next examined whether both domains were required for recruiting transcriptional machinery to N-myc condensates. Here we applied a chemogenetic tool named SPARK-ON or SparkDrop (since the droplets formed via SPARK-ON are called SparkDrop) to drive phase separation of both N-myc mutants (Fig. 5a, Supporting Fig. S4)⁴¹. SparkDrop drives protein phase separation by induction of multivalent interactions with the small molecule lenalidomide. Briefly, SparkDrop is based on the newly engineered protein pair CEL (109 amino acids [aa]) and ZIF (31aa), which, upon addition of lenalidomide (lena), form a heterodimer (CEL···lena···ZIF). To induce PS, we fused the N-myc mutants to mEGFP and CEL (N-myc-mEGFP-CEL). To incorporate multivalency, we utilized a *de novo* designed coiled coil that is a homo-tetramer (HOTag6)^{60,61}. We fused ZIF, a nuclear localization signal (NLS), and a non-green fluorescent EGFP mutant (EGFP-Y66F) to HOTag6 (ZIF-NLS-EGFP(Y66F)-HOTag6). Hence, treatment with lenalidomide drives oligomerization of N-myc and induces phase separation even at concentrations that are below the saturation concentration of N-myc.

First, we demonstrated that SparkDrop induced phase separation of TAD-deleted N-myc¹³⁸⁻⁴⁶⁴ upon addition of lenalidomide (Fig. 5a, Supporting Fig. S5). The condensates recruited the DNA-binding partner MAX as expected (Fig. 5b). In contrast, most of the N-myc condensates did not contain MED1 (Fig. 5c, d) or Pol II S5p (Supporting Fig. S6). These data thus show that the TAD domain is critical for recruitment of the transcriptional machinery to N-myc condensates.

Next, we showed that SparkDrop was also able to drive phase separation of bHLH-LZ-deleted N-myc¹⁻³⁶⁵ (Fig. 5e, Supporting Fig. S5). The majority of these condensates contained no MED1 or Pol II S5p (Fig. 5f, g, Supporting Fig. S6), suggesting that they are largely inactive for gene transcription. As expected, these condensates contained no MAX (Fig. 5g). Therefore, our data show that the DNA-binding domain is also critical for assembling transcriptionally active N-myc condensates. Together, our results indicate that the TAD and the DNA-binding domains are both required to recruit the transcriptional machinery, and that condensate formation itself is not automatically sufficient.

The SparkDrop tool decouples N-myc PS from protein abundance

We demonstrated that SparkDrop enabled us to drive PS without changing protein levels, thus decoupling phase separation from a need to increase protein abundance. We tagged N-myc with SparkDrop (N-myc/SparkDrop). We first explored the response of N-myc/SparkDrop-expressing cells to treatment with lenalidomide. Lenalidomide activated SparkDrop and induced condensate formation within 6 – 10 minutes (Fig. 6a). The total fluorescence of N-myc showed little change during that time, suggesting that N-myc protein levels were constant in the nucleus. DMSO alone did not induce N-myc phase separation, and lenalidomide could not drive N-myc phase separation in the absence of the HOTag6. Furthermore, without N-myc, SparkDrop did not form condensates even upon addition of lenalidomide (Supporting Fig. S7). We also demonstrated that in the absence of lenalidomide, N-myc/SparkDrop undergoes PS with a saturation concentration of ~330

– 400 nM (Extended Data Fig. 9a), similar to that of N-myc-mEGFP, indicating that the SparkDrop tag itself had little effect on N-myc's phase behavior. Lenalidomide-induced SparkDrop shifts the saturation concentration to ~ 150 nM (Extended Data Fig. 9a). This indicates that N-myc/SparkDrop has an operating concentration at around 180–300 nM, in which N-myc is diffusive in the absence of lenalidomide and forms condensates upon addition of lenalidomide. Indeed, the stably expressing cell line expressed N-myc/SparkDrop at around 200 nM (Methods, Extended Data Fig. 9b). Lastly, we showed that N-myc/SparkDrop condensates were able to fuse and coalesce, indicating that they are fluid droplets with an inverse capillary velocity of 1.31 ± 0.29 (s/ μ m), which is similar to that of N-myc-mEGFP (Supporting Fig. S8).

Next, we tested whether N-myc/SparkDrop condensates bear the hallmarks of transcriptional activity. First, the N-myc/SparkDrop condensates contained the DNA-binding and dimerization partner MAX (Fig. 6b, f). Second, the N-myc/SparkDrop condensates contained transcriptional machinery including MED1 and Pol II S5p (Fig. 6c, d, f). Lastly, the N-myc/SparkDrop condensates contained nascent RNA (Fig. 6e, f). These data thus show that SparkDrop is an appropriate tool to form condensates with the hallmarks of those formed by N-myc but can do so without changing the protein concentration. Therefore, it allows us to decouple the effect of phase separation on N-myc-mediated transcription and function from the effect of increasing N-myc levels.

As a first step in this direction, we tested whether N-myc phase separation had an effect on cell proliferation. Our data indicated that the SH-EP cell proliferation was increased by $15 \pm 4\%$ when N-myc/SparkDrop expressing cells were treated with lenalidomide as compared to the DMSO-treated cells (Fig. 6g). In cells expressing the N-myc/SparkDrop control without the HOTag6, lenalidomide had no effect on cell proliferation. Therefore, SparkDrop-induced phase separation of N-myc leads to a significant proliferation advantage for cells, even at the same N-myc concentration (Fig. 6a, h, i).

PS of N-myc regulates gene transcription

Next, we examined whether lenalidomide/SparkDrop-induced phase separation of N-myc regulated gene transcription. We chose two key N-myc-regulated genes that are known for their oncogenic character in promoting cell proliferation, serine incorporator 2 (*SERINC2*) and annexin A8 (*ANXA8*)^{62,63}, and tested whether their transcription was altered upon N-myc phase separation. First, RT-qPCR analysis of *SERINC2* mRNA levels for cells treated with the compounds for different duration indicated that the mRNA levels in cells treated with lenalidomide for 16 hours showed a significant increase compared to 4- or 8-hour treatment (Extended Data Fig. 10) Thus, we treated the samples with the compound for 16 hours for the following experiments. RT-qPCR analysis showed that the mRNA levels of *SERINC2* and *ANXA8* were significantly higher for cells with N-myc condensates (incubated with lenalidomide for 16 hours) than for cells without condensates (incubated with DMSO for 16 hours) (Fig. 6j). Lastly, lenalidomide treatment of cells expressing the N-myc/SparkDrop control without HOTag6 did not result in increased transcription (Fig. 6j). Therefore, our data indicate that the process of N-myc phase separation enhances

transcriptional activity of key proliferative genes, in agreement with our results that phase separation also promotes proliferation of SH-EP cells.

Phase-separated N-myc regulates the transcriptome

We then examined the effect of phase-separated N-myc (induced by lenalidomide/SparkDrop) on the transcriptome without changing N-myc abundance in the nucleus (Fig. 7a). We treated the N-myc/SparkDrop-expressing cells with and without lenalidomide, followed by RNA-seq.

First, we determined whether SparkDrop tag itself changed the core transcriptional role of N-myc. We examined a previously established list of 41 core Myc-dependent genes⁶⁴ and observed that 38 out of 41 were expressed following N-Myc/SparkDrop expression in SH-EP cells without treatment with lenalidomide while no expression of these genes were detected in control SH-EP cells (no N-myc expression) (Fig. 7b). This suggested that the SparkDrop system caused little perturbation to the core transcriptional function of N-myc and was thus appropriate to use.

Second, we tested the effect of SparkDrop-tagged N-myc in the absence of lenalidomide on the transcriptome. Differentially expressed genes (DEGs; p-value < 0.01, |Log₂FC| 0.58, FDR < 0.1) were determined, which revealed a change of gene expression upon N-myc/SparkDrop expression. We identified ~6900 DEGs with transcriptional changes 1.5-fold, including ~3100 genes that were up-regulated and ~3800 genes that were down-regulated (Supporting Fig. S9, Supporting Excel File 1), consistent with previous studies of the effect of N-myc-expression on gene transcription^{65,66}. Analysis by gene ontology (GO) enrichment shows that the DEGs are associated with many N-myc-regulated biological processes including ribosome biogenesis (Supporting Fig. S10). Furthermore, we demonstrated that the CEL tag has little effect on N-myc's transcriptional activity by comparing RNA-seq data from the cells expressing N-myc-mEGFP-CEL versus N-myc-mEGFP (Supporting Fig. S11–12). Therefore, our results indicate that SparkDrop results in little or no perturbation of the N-myc transcriptional function and that N-myc-mEGFP-CEL activates known transcriptional programs also in SH-EP cells.

Third, we examined whether phase-separated N-myc induced by lenalidomide/SparkDrop modulates the N-myc transcriptome. We determined transcriptomic changes following lenalidomide treatment of N-myc/SparkDrop-expressing cells (relative to the control cells without N-myc/SparkDrop). ~6700 DEGs (p-value < 0.01, |Log₂FC| 0.58, FDR < 0.1) were identified with changes to gene expression 1.5-fold, including 3025 up-regulated genes and 3636 down-regulated genes (Fig. 7c, Supporting Excel File 2). This result is consistent with our imaging data that the N-myc/SparkDrop condensates contain transcriptional machinery (Fig. 6b – e). Analysis by GO enrichment indicates that the phase separated-N-myc modulates multiple known biological processes, including ribosome biogenesis (Fig. 7d)^{65,66}.

Selective transcriptomic regulation by MYCN PS via SparkDrop

We then decided to examine transcriptional differences between cells with diffuse N-myc/SparkDrop expression (without lenalidomide treatment and thus no phase separation)

and cells with phase-separated N-myc/SparkDrop (with lenalidomide treatment), i.e., the contribution of phase separation to transcription in addition to the transcriptional output of diffuse N-myc at the same concentration. Cells not treated with lenalidomide have no condensates, whereas lenalidomide-treated cells contain condensates. DEGs (p -value < 0.01 , $|\text{Log}_2\text{FC}| \geq 0.58$, $\text{FDR} < 0.1$) were determined based on the RNA-seq data of the N-myc/SparkDrop-expressing cells with and without lenalidomide. We found 99 DEGs that were differentially expressed with transcript level change ≥ 1.5 -fold, including 88 genes that were up-regulated and 11 genes that were downregulated (Fig. 7e, f, Supporting Excel File 3, Supporting Fig. S13). These 88 genes are modulated by N-myc phase separation (induced by SparkDrop). In contrast, lenalidomide treatment in engineered cells expressing the N-myc/SparkDrop control without HOTA6 had little effect on transcriptional activity; only 10 DEGs were identified and none of them overlapped with the N-myc PS-regulated genes when we compared the RNA-seq data of lenalidomide versus DMSO-treated cells (Supporting Excel File 4).

In particular, several genes that are upregulated by expression of diffuse N-myc are further upregulated in cells with phase-separated N-myc. This shows that 1) they are up-regulated by diffuse N-myc (in comparison to the control); 2) their transcriptional expression is increased further by phase separation of N-myc. This is consistent with the qRT-PCR data (Fig. 6j). In total, SparkDrop-induced phase separation of N-myc enhances transcription of $< 3\%$ of the upregulated genes. Among the genes that are down-regulated upon diffuse N-myc expression, several are further down-regulated upon phase separation of N-myc. In total, phase separation suppresses transcription of $< 1\%$ N-myc-repressed genes. The corollary of these findings is that the transcription of most genes is not impacted by SparkDrop-induced N-myc phase separation. Therefore, phase separation of N-myc does not influence transcription for the majority of N-myc-regulated genes. Importantly, many of the genes up-regulated by N-myc PS are oncogenes. On the other hand, many of the genes down-regulated by N-myc PS are tumor suppressors. N-myc phase separation via SparkDrop alters the expression of a small subset of Myc-responsive genes, but these are enriched with genes that have been reported to promote cell proliferation, which may connect the role of N-myc PS in gene regulation to its role in promoting proliferation.

Discussion

In this work, we discovered that N-myc forms condensates via phase separation, which requires the N-terminal disordered region, as well as the c-terminal bHLH domain that binds MAX and DNA. Furthermore, these N-myc condensates contain transcriptional machinery including MED1, Pol II and nascent RNA, in addition to the obligate DNA-binding partner MAX. Our in vitro studies using purified proteins indicate that N-myc phase separation requires MAX interaction and E-box DNA binding. Therefore, our results demonstrate that the N-myc condensates are transcriptionally active.

To examine the role of N-myc phase separation in gene regulation, we applied a powerful chemogenetic tool, SparkDrop (i.e. SPARK-ON)⁴¹, that allows us to induce phase separation without changing expression levels of the driver of phase separation, here N-myc, since expression levels of TFs are known to affect gene expression. Treatment

with lenalidomide to activate SparkDrop and induce phase separation of N-myc in the neuroblastoma SH-EP cell line left N-myc levels in the nucleus unchanged but resulted in rapid formation of condensates on a timescale of 10 minutes. These condensates appeared at genomic loci of N-myc-responsive genes, recruited MAX, transcriptional machinery and contained nascent RNA; hence, they have the hallmarks of active transcriptional condensates. We also observed that both the dilute and phase-separated states regulated core Myc-responsive genes. On the other hand, comparing cells with the SparkDrop-enabled phase-separated state and the diffuse state, we observed that most Myc-regulated genes do not experience expression alterations upon N-myc phase separation. Only ~3% of genes that are upregulated by Myc expression are further up-regulated upon phase separation. <1% of Myc-downregulated genes are further down-regulated upon phase separation. Our analysis shows that these DEGs are enriched with oncogenes and tumor suppressors, respectively, and that this mechanism may therefore contribute to oncogenesis. Thus, our data suggest a correlation between the role of N-myc PS in gene regulation and its role in cell proliferation. However, this does not necessarily indicate a causal relationship, which will require additional evidence by approaches such as genetic knock-out or knock-down of specific genes. On the other hand, our results clearly show that diffuse N-myc complexes with MAX and the transcriptional machinery are able to mediate transcriptional function. For most N-myc-regulated genes, phase separation is simply a consequence of high N-myc expression rather than a state that modulates function broadly, except for a small subset of the N-myc-regulated genes.

Our work indicates that the chemogenetic tool SparkDrop provides a new approach to dissect role of phase separation for proteins that form condensates. However, potential perturbation to the protein of interest by the SparkDrop should be carefully examined. For example, for a transcription factor, it should first be demonstrated that this tag does not block the transcriptional activities.

Many transcription factors have been reported to undergo phase separation that influences transcription, and transcriptional condensates have been shown to affect normal development⁶⁷ and contribute to pathogenesis^{30,33,38,68,69}. However, one key question is: Does phase separation confer unique transcriptional functions in comparison to diffuse complexes? Here our work indicates that phase separation differentially regulates transcription and partially promotes proliferation. In particular, PS affects transcription of a small portion of N-myc-regulated genes, reminding us that biological functions should only be assigned to condensates with specific evidence. Our data reveals the transcriptional activity of N-myc condensates that bind target genes, recruit transcriptional machinery, and contain nascent RNA. Furthermore, N-myc's transcriptional activity is similar between the phase-separated state and the diffuse state, at the same total N-Myc abundance in the nucleus. While the formation of condensates resulting from protein concentration increase may recruit additional proteins and thus enhance biological function, based on our work, one could predict that the same increase in protein abundance without condensation would lead to a similar functional enhancement. Biomolecular condensates have emergent properties, and reports of their functions include triggering reactions⁷⁰, noise filtering^{71,72} and translational pattern changes⁷³ but to characterize the functions of condensates, e.g.

compared to those of soluble complexes, needs dissociation of function experiments and quantitative characterization⁷⁴.

How and why does N-myc phase separation affect a small proportion of genes? These effects could be attributed to unique physical properties of condensates, e.g. their coalescence capacity, which is absent in diffuse complexes of which the size distribution is constant at a given concentration and does not increase over time³⁵. Transcriptional condensates may modify chromatin structure via coalescence that could recruit genes with potent enhancers, altering their expression³³. While these effects may further enhance over time as the elevated expression of TFs persists, our data indicates that the dynamic disassembly and assembly of N-myc condensates during cell cycle limits the lifetime of condensates and that their function could therefore be naturally restrained.

In conclusion, our work shows that phase separation of N-myc differentially regulates transcription and does not influence a large percentage of the MYC-regulated genes. This is consistent with our work on a YAP fusion oncoprotein, which also reveals differential role of phase separation in transcription by this oncoprotein transcription factor⁷⁵. Nevertheless, targeting oncoprotein condensates may represent a therapeutic approach because small molecule inhibitors could be concentrated within these compartments via direct binding to the targets or by interacting with other elements in the condensates, as well as possible solubility effects^{38,39}. Whether such a therapeutic strategy would be successful likely depends on the fraction of N-myc within condensates. This is ~30–50% N-myc within condensates in our experiments and may be a higher fraction in cancers with high overexpression of Myc due to copy number changes, chromosomal translocations, or upstream oncogenic signaling^{3–5}.

Methods

Plasmid construction.

N-myc was cloned from the cDNA. Its truncation mutants were later obtained via PCR. MAX was cloned from The CCSB Human ORFeome Collection (donated by Marc Vidal). The red fluorescent protein mKO2 was a gift from Drs. Michael Davidson & Atsushi Miyawaki via Addgene (Plasmid # 54625). Its mutant mKO3 was engineered by introducing the M176F mutation into mKO2 to improve fluorescence in cells as previously described^{76,77}. N-myc-mEGFP, N-myc¹⁻³⁶⁵-mEGFP, N-myc¹³⁸⁻⁴⁶⁴-mEGFP, MAX-mKO3 were created by linking the DNA sequence of N-myc and its truncations to mEGFP, MAX to mKO3 with a 10-AA GSSGGSGGGT linker. To create N-myc-mEGFP-CEL fusions, CEL was amplified from full length CRBN and cloned into N-myc-mEGFP plasmid, with a 10-AA linker between mEGFP and CEL. The full-length N-myc was replaced with its truncations resulting in N-myc¹⁻³⁶⁵-mEGFP-CEL and N-myc¹³⁸⁻⁴⁶⁴-mEGFP-CEL. All the sequences were cloned into pHR_SFFV (Addgene plasmid #79121) vector by digestion with restriction enzyme followed by ligation and confirmation using sequencing. All constructs in this study are listed in Table S1.

Cell culture.

SH-EP (University of California, San Francisco, Cell and Genome Engineering Core) cells were cultured at 37 °C and 5% CO₂ in Dulbecco's Modified Eagle medium (DMEM) plus high glucose with heat-inactivated Fetal Bovine Serum (FBS) at a concentration of 10% with streptomycin (100 µg/mL), and penicillin (100 units/mL). Kelly (Sigma-Aldrich 92110411), CHP134 and CLB-GA (Childhood Cancer Repository, Children's Oncology Group resource laboratory) cells were cultured at 37 °C and 5% CO₂ in Roswell Park Memorial Institute (RPMI) 1640 Medium, supplemented with 10% heat-inactivated Fetal Bovine Serum (FBS). All culture supplies were obtained from Gibco.

Lentivirus preparation.

N-myc-mEGFP, N-myc (full-length or truncated)/SparkDrop, N-myc/SparkDrop control (no HOTag6), MAX-mKO3, H2B-mIFP, H2B-mCherry and mEGFP lentiviral plasmids were co-transfected with pAX2 and pVSVG at 3:2:1 ratio into HEK293T cells using polyethylenimine (MilliporeSigma 764965). Lentiviruses were harvested after 48 hours.

Fluorescence microscopy.

Cells were imaged by an inverted confocal microscope (Nikon Eclipse Ti, plus a Yokogawa CSU-W1 confocal scanner unit, ORCA-Flash4.0 (Hamamatsu) that is a CMOS camera, ASI MS-2000 XYZ automated stage (Applied Scientific Instrumentation). The microscope was equipped with several objectives including Nikon Plan Apo λ 20X air (N.A. 0.75), Nikon Apo TIRF 60X oil (N.A. 1.49) and CFI Plan Apo λ 100X oil (N.A. 1.45). The confocal microscope was also equipped with several laser lines (Integrated Laser Engine (Spectral Applied Research), including 405, 488, 561, and 640 nm lasers (Coherent). The confocal scanning unit contains several emission filters, including 460/50, 525/50, 610/60 and 732/68 nm. The NIS-Element Ar Microscope Imaging Software (Nikon) was used to capture the images.

Live cell imaging.

SH-EP cells were grown in glass-bottom 8-well chambers (Thermo Scientific 155411). Lentiviral infection was done at ~70% confluency of cells. Imaging was carried out 24h after viral infection. Time-lapse imaging was carried out in an environmental control unit incubation chamber (InVivo Scientific) at 37 °C and 5% CO₂. For imaging mitosis, 100 µM ascorbic acid was added to increase mitotic index. Lenalidomide (Ark Pharma, AK-47482) were carefully added to the cells in the incubation chamber when the time-lapse imaging was started. NIS-Elements Microscope Imaging Software (Nikon) was used for image acquisition. Images were processed using NIS-Elements and ImageJ (NIH). Chromosome volume was calculated based on the near infrared fluorescence from H2B-mIFP or 1 µg/mL Hoechst 33342 staining. The fusion events of the N-myc condensates and N-myc/SparkDrop condensates were analyzed by calculating the aspect ratio of the fusing condensates over time using imageJ. Droplet size and amount were analyzed using the 3D Objects Counter function in ImageJ.

mEGFP fluorescence intensity-concentration relationship.

mEGFP protein was purified. To measure the concentration, the absorbance at 488 nm was evaluated using Thermo scientific nanodrop 2000C. The concentration was obtained by dividing the absorbance value by the extinction coefficient. We then diluted the proteins between 0.037 μM and 2.35 μM . These protein samples were imaged under the microscope with the same parameters as cells. The intensity of the laser was measured (Thorlabs PM100D). The same procedure was repeated for N-myc-mEGFP.

Phase separation curves and other thresholding methods.

SH-EP cells expressing N-myc-mEGFP or N-myc/SparkDrop were stained with 1 $\mu\text{g}/\text{mL}$ Hoechst 33342 for 10 minutes. The cells were imaged under a spinning disc confocal microscope with 100X objective. We sectioned the nucleus into multiple slices. To obtain the curve for phase separation, we used 3D Objects Counter of ImageJ. We set a fluorescence intensity threshold so that the nuclei were selected. Next we calculated the nuclear mean fluorescence intensity. The N-myc-mEGFP concentration was then estimated by comparing the intensity to the mEGFP concentration-fluorescence intensity curve (see above). The N-myc-mEGFP condensates were selected by setting a higher threshold, which is about twice of the average concentration and further adjusted for each cell until all condensates (but not additional area) was selected. The final threshold is between 1.8 and 2.2 times of the average concentration. We calculated the total fluorescence intensity of condensates for each nucleus. SPARK value was calculated as the ratio of the total condensate fluorescence intensity over the whole nucleus fluorescence intensity, and plotted to obtain the phase separation curves with saturation concentrations.

To further confirm the phase separation saturation concentration, two other methods without manually adjusted threshold were included. In the first method, the maximum and average pixel intensities across the nucleus were measured. Nuclei were defined as ‘with condensates’ when maximum/average ≥ 2 , or “no condensates” when maximum/average < 2 . This cutoff was selected as it included $>95\%$ cells with visible condensates and also excluded $>95\%$ cell without visible condensates. Average concentrations of nuclei were plotted. In the second method, cells were segmented by cellpose model and filtered by aberrant size (area size was within 3000 and 7000 pixels). Then the granularity texture was profiled by Granularity module from CellProfiler (v4.6). The key parameter of radius structure element was set to match the condensate size in nuclei (radius = 6). The second vector values were used for plotting and evaluation of phase separation saturation values.

Immunofluorescence.

SH-EP cells were cultured in a glass-like-bottom 96 well plate, infected with N-myc-mEGFP (full-length or truncated) or N-myc/SparkDrop viruses, and fixed with 4 % paraformaldehyde in PBS at 24 hours post-infection. SH-EP cells were permeabilized with PBST (0.1% Triton X-100 in PBS) and blocked with 2% BSA and 10% goat serum in PBS for 30 minutes. The cells were next incubated with primary antibodies in blocking buffer. After washing three times with PBST, the cells were incubated with secondary antibodies at room temperature for 1 hour. After washing three times with PBST, 100 μL of PBS + 1 $\mu\text{g}/\text{mL}$ Hoechst 33342 was added to each well and the cells were imaged after 10 minutes.

Kelly, CHP134, SH-EP and CLB-GA cells were grown on glass coverslips in 6-well plates for 24 hours. The cells were fixed with 4 % paraformaldehyde in PBS, permeabilized with PBST (0.1% Triton X-100 in PBS) and blocked with 5% normal goat serum in PBST for 30 minutes. The cells were incubated overnight with anti-MYCN antibody in blocking buffer at 4 °C. After washing three times with PBST, the cells were incubated with secondary antibodies at room temperature for 1 hour, then mounted onto glass slides using mounting media with DAPI (Vectashield H-1800). Detailed antibody information, incubation time and temperature are listed below:

antibody	Brand and catalog	dilution	Incubation time	Incubation temperature
Anti-MED1 antibody (for SH-EP cells)	Santa Cruz sc-74475	1:1000	2.5 hours	RT
anti-RNA polymerase II CTD repeat YSPTSPS (phospho S5) antibody	Abcam ab5408	1:200	overnight	4 °C
Anti-N-myc antibody	Cell Signaling 9405S	1:100	overnight	4 °C
Anti-MED1 antibody (for Kelly cells)	Abcam ab64965	1:50	overnight	4 °C
Anti-MycN antibody (only for co-localization with MED1 in Kelly cells)	Santa Cruz sc-53993	1:100	overnight	4 °C
Anti-c-Jun antibody	Cell Signaling 9165S	1:100	overnight	4 °C
Anti-rabbit IgG Fab2 Alexa Fluor 647-conjugated secondary antibodies	Cell Signaling 4414S	1:200	1 hour	RT
Anti-rabbit IgG Fab2 Alexa Fluor 488-conjugated secondary antibodies	Cell Signaling 4412S	1:200	1 hour	RT
Anti-mouse IgG Fab2 Alexa Fluor 488-conjugated secondary antibodies	Cell Signaling 4408S	1:200	1 hour	RT
Anti-mouse IgG H&L Alexa Fluor 555-conjugated secondary antibodies	Abcam ab150114	1:200	1 hour	RT

Colocalization analysis.

For the colocalization images in SH-EP and Kelly cells, we used the Hoechst signal to select each nucleus area without nucleoli, and plot values of each pixel in each channel of the selected areas using an ImageJ macro. Pearson correlation coefficient was calculated using the plotted values. For each experiment, we analyzed three biologically independent replicates with 20 cells for each replicate.

Pol II S5P and MED1 condensate numbers.

Pol II S5P and MED1 condensates were analyzed using ImageJ. The z-stack images were max-projected. For each cell, the condensates in the nucleus were selected using a threshold of 1.6 times of the average stained fluorescence intensity in the nucleus. The total count of selected areas bigger than $0.05 \mu\text{m}^2$ were considered as the condensate number.

DNA FISH.

SH-EP cells were cultured in a glass-like-bottom 96 well plate, infected with the N-myc-mEGFP virus, and imaged for green fluorescence. The cells were then fixed in 3:1 methanol/acetic acid and dried, immersed in 2x Saline Sodium Citrate (SSC) (PH 7.0) for 2 minutes at room temperature (RT), dehydrated in an ethanol series (70%, 85% and 100%), each for 2 minutes at RT and dried. *TP53* FISH probes (Cytocell LPH571-A) and the plate were prewarmed at 37°C for 5 minutes. 50 µL probes were added to the well and denatured at 75°C for 2 minutes, followed by hybridization at 37°C overnight. PBS was added to surrounding wells to ensure a humid environment. After hybridization, the well was immersed in 0.4x SSC at 72°C for 2 minutes and 2xSSC + 0.05% Tween-20 at RT for 30 seconds. 100 µL of PBS was added to the well. The samples were imaged after 15 minutes.

Nascent-RNA labelling.

We labeled the nascent RNA with a Click-iT RNA kit (Thermo Fisher, C10330). SH-EP and Kelly cells were plated on an 8-well chambered cover glass (Thermo scientific 155411). SH-EP cells were infected with N-myc-mEGFP or N-myc/SparkDrop lentiviruses. SparkDrop-infected SH-EP cells were incubated with 1 µM lenalidomide for 2 hours to induce condensate formation. After labeling with 1 mM 5-ethynyl uridine (EU) for 1 hour, we fixed cells with paraformaldehyde (4%) in PBS and permeabilized the cells with PBST (0.5% Triton X-100 in PBS) and incubated the cells with Click-iT reaction cocktail for 30 min (room temperature), followed by visualization of 5-ethynyl uridine. We detected nascent RNA by incubating cells with the uridine analog 5-ethynyluridine (EU). One hour of incubation incorporated EU into newly transcribed RNA, which was detected with red fluorescent dyes⁷⁸.

Immunofluorescence imaging and staining in Kelly cells.

Immunofluorescence imaging of the endogenous N-myc was also conducted in Kelly cells using the above approach. We also stained other TFs such as c-Jun.

Western blot and estimation of protein levels.

For detecting N-myc protein levels, we lysed the cells using lysis buffer (Cell signaling 9803S) (100 µL) for 1 minute (room temperature). Then we mixed the sample with NuPAGE (NP0009) (15 µL) plus NuPAGE LDS (NP0007) (37.5 µL). Next, the samples were incubated for 10 minutes (70°C). We analyzed the samples on NuPAGE 4–12% Bis-Tris gel (NP0336). Next we transferred the samples to a nitrocellulose membrane in a Bio-rad Trans-Blot Turbo machine for 45 min (under 25 V). We blocked the membrane in 5% non-fat milk for 1 hour (room temperature), and incubated the samples with an N-myc mouse monoclonal antibody (Santa Cruz sc-53993, 1:2000) overnight (4°C). This was followed by 3 washes in PBST (0.1% Tween-20 in PBS) (5 minutes each). The samples were then incubated with an HRP-conjugated anti-mouse secondary antibody (Cell signaling 7076S, 1:5000), followed by 3 washes (5 min each). We added HRP chemiluminescent substrate (Thermo scientific 34580) to the membrane, followed by incubation for 5 minutes (room temperature). Lastly, we imaged the samples under the Bio-rad Chemidoc XRS system or

Prometheus 30–507L (film exposure). To stain β -actin, we used its primary antibody (Santa Cruz sc-47778) with 1-hour incubation at room temperature (1:5000 dilution).

To estimate endogenous N-myc protein concentration in Kelly cells, we compared Kelly cells with the stable SH-EP cells expressing N-myc-mEGFP (SH-EP-MYCN) (see Supporting Fig. S7). First, we performed a western blot to compare protein abundance. ~1000 cells were collected for the western blot. The bands were analyzed using ImageJ. Second, Kelly and SH-EP-MYCN were grown in a 8-well chamber (Thermo Scientific 155411). We then stained the cells with Hoechst 33342 (1 μ g/mL) for 10 minutes, and imaged them under the confocal microscope with the 100X objective. We sectioned the nucleus into multiple slices (0.5 μ m interval). We calculated the nuclear volume using ImageJ (3D Objects Counter). Third, the green fluorescence was collected for the SH-EP-MYCN cells. We used the green fluorescence intensity to calculate the N-myc-mEGFP concentration, using the purified mEGFP concentration-fluorescence intensity curve (Supporting Fig. S6). We estimated the Kelly cell N-myc concentration by comparing the intensity of the western-blot band ⁷⁹, the nuclear volume of Kelly vs SH-EP-MYCN cells, and the N-myc-mEGFP concentration in the nucleus of SH-EP-MYCN cells.

MAX knock-out.

Guide RNA sequence GAGCGATAACGATGACATCG targeting MAX was cloned into LentiCRISPRv2. SH-EP cells were infected with the lentivirus and selected using puromycin. Knock-out effect in pooled cells were confirmed by western blot (antibody CST #4739, 1:1000) following similar procedure as N-myc.

Sequence of N-myc, Max constructs and DNA oligonucleotides for in vitro assays.

Labeled (Alexa488) and unlabeled DNA oligonucleotides were synthesized by Integrated DNA Technologies, Inc. (IDT, USA). The sequences of proteins and DNA oligonucleotides used in the current study are provided in the table below:

Protein	Sequence (amino acid)
N-myc	MPSCSTSTMPG MICKNPDLEFDSLQPCFY PDEDDFYFGGPDSTPPGEDIW KKFELLPTTP LSPSRGFAEHSSEPPSWVTE MLENELWGS PAEEDAFGLG GLGGLTPNV ILQDCMWSGF SAREKLERAV SEKLQHGRGPPTAGSTAQSP GAGAASPAGRGHGGAAGAGR AGAALPAELA HPAAECVDP A VVFPFPV NKR EPAPVPAAPA SA PAAGP AVA SGAGIAAPAG APGVA PPRPGGRQTSGGDHK ALSTSGEDTL SDS DDEDEDEEED EEEIDVV TVEKRRSSSNTKAVTFTIT VRPKNAALGPGRAQSSELIL KRCLPIHQHNYAAPSPYVESEDAPPQKKI KSEASPRPKSVIPPKAKSL SPRNSDSED SERRRNHNILERQRRNDLRSS FLTLRDHVPE LVKNEKAAK V VILKKATEYV HSLQAEHQQL LLEKEKLQAR QQQLLKKIEH ARTC
Max	MSDNDIEVESDEEQPRFQS AADKRAHHNA LERKRRDHKDSFHSLRDSV PSLQGEKASR AQILDKATEY IQYMRKNHT HQQDIDDLKRQNALLEQQVR ALEKARSSAQ LQTNYPSSD NSLYTNAKGST ISAFDGGSDSSSESEPEEPQ SRKKLRMEAS
DNA oligonucleotides	Sequence (nucleotide)
1Ebox (26 mer)	5' AGCTTAACTGACCACGTGGTCAACTA 3
3Ebox (78 mer)	5' AGCTTAACTGACCACGTGGTCAACTA AGCTTAACTGACCACGTGGTCAACTA AGCTTAACTGACCACGTGGTCAACTA 3'

Protein	Sequence (amino acid)
7Ebox (182 mer)	5' AGCTTAACTGACCACGTGGTCAACTA AGCTTAACTGACCACGTGGTCAACTA AGCTTAACTGACCACGTGGTCAACTA AGCTTAACTGACCACGTGGTCAACTA AGCTTAACTGACCACGTGGTCAACTA AGCTTAACTGACCACGTGGTCAACTA AGCTTAACTGACCACGTGGTCAACTA 3'
1 NC Ebox-TA (26 mer)	5' AGCTTAACTGACCATCTGGTCAACTA 3'
1 NC Ebox-TC (26 mer)	5' AGCTTAACTGACCATATGGTCAACTA 3'
7 NC Ebox-TA (182 mer)	5' AGCTTAACTGACCATCTGGTCAACTA AGCTTAACTGACCATCTGGTCAACTA AGCTTAACTGACCATCTGGTCAACTA AGCTTAACTGACCATCTGGTCAACTA AGCTTAACTGACCATCTGGTCAACTA AGCTTAACTGACCATCTGGTCAACTA AGCTTAACTGACCATCTGGTCAACTA 3'
7 NC Ebox-TC (182 mer)	5' AGCTTAACTGACCATATGGTCAACTA AGCTTAACTGACCATATGGTCAACTA AGCTTAACTGACCATATGGTCAACTA AGCTTAACTGACCATATGGTCAACTA AGCTTAACTGACCATATGGTCAACTA AGCTTAACTGACCATATGGTCAACTA AGCTTAACTGACCATATGGTCAACTA 3'
Non-Ebox (182 mer)	5' AGCTTAACTGACTTAGCAGTCAACTA AGCTTAACTGACTTAGCAGTCAACTA AGCTTAACTGACTTAGCAGTCAACTA AGCTTAACTGACTTAGCAGTCAACTA AGCTTAACTGACTTAGCAGTCAACTA AGCTTAACTGACTTAGCAGTCAACTA AGCTTAACTGACTTAGCAGTCAACTA 3'

Expression and purification of N-myc & Max proteins.

The sequences for human N-myc and Max proteins were synthesized (Thermo Fisher Gateway cloning) along with a coding sequence for an N-terminal TEV protease cleavage site (ENLYFQGS) including 5' and 3' attB sites for cloning into expression vectors. The sequences were codon optimized for expression in an *E. coli* system. The sequences from the pDONR221 vector were transferred using Gateway™ LR Clonase™ Enzyme mix (Invitrogen, USA) to the expression vector pDEST17 (Thermo Fisher, USA), containing N-terminal 6xHis-tag sequence. Both proteins were expressed in *E. coli* strains [BL21(DE3) pLysS for Myc and BL21-Gold(DE3) for Max]. Cultures were grown to an OD₆₀₀ = 0.8 and induced with 1 mM IPTG followed by overnight expression at 18 °C. Pelleted cells were resuspended in 50 mM Tris pH 7.5, 1M NaCl, 30 mM Imidazole and 5 mM β-mercaptoethanol. Further, the pellets were lysed using sonication on ice. Cell lysates were centrifuged and insoluble inclusion bodies were collected. The inclusion bodies were solubilized in a buffer containing 20 mM Tris pH 7.5, 6 M GdmHCl, 50 mM NaCl, 50 mM Imidazole and 5 mM β-mercaptoethanol overnight at 4°C.

Solubilized inclusion bodies were cleared by centrifugation at 25,000 × g and supernatants were loaded onto columns of Chelating Sepharose Fast Flow™ resin (GE Healthcare, USA) charged with nickel sulfate. The columns were washed with 3 column volumes of 20 mM Tris pH 7.5, 4 M urea, 50 mM imidazole. Protein elution from the Ni-NTA resin was done using 4 M urea, 20 mM Tris pH 7.5, 500 mM imidazole. The eluted proteins were used to

cleave the 6xHis-tag by TEV cleavage in 20 mM Tris pH 7.5, 2 M urea, 50 mM NaCl, 0.5 mM EDTA, 1 mM DTT buffer, overnight at 4°C. The cleaved proteins were passed over Ni-NTA columns and the flowthrough and wash fractions were collected. The proteins were concentrated using Amicon centrifugal filters (3,000 MWCO). The proteins were further purified using a S75 Superdex size exclusion column (GE Healthcare, USA) with buffer containing 20 mM Tris pH 7.5, 2 M GdmHCl, 50 mM NaCl and 1 mM TCEP. The identity of the proteins was confirmed using intact mass spectrometry. N-myc and Max were stored in a denaturing buffer with 4 M GdmHCl, 20 mM Tris pH 7.5, 50 mM NaCl and 1 mM TCEP at 4°C. The molar absorptivity of N-myc and Max were taken as 29520 M⁻¹ cm⁻¹ and 5960 M⁻¹ cm⁻¹, respectively.

Refolding of Myc and Max proteins.

Both N-myc and Max proteins were individually refolded using serial steps of dialysis as previously reported⁸⁰. The proteins were dialyzed in Spectra/Por 3 (3.5 kD MWCO) Dialysis Tubing (Fisher Scientific, USA). Buffer containing 20 mM HEPES pH 7.5, 50 mM KCl, 10 mM MgCl₂ and 1 mM DTT with decreasing levels of urea was used for dialysis during each refolding step (4 M urea, 2 M urea, 1 M urea; each step for 1h) at 4°C. In the final step, buffer with 20 mM HEPES pH 7.5, 50 mM KCl, 10 mM MgCl₂, and 1 mM DTT was used for overnight dialysis at 4°C. The refolded N-Myc and Max proteins were used in a 3:1 ratio for all assays. The proteins were freshly refolded for each experiment. We refolded N-myc and Max independently and mixed them at a molar ratio of 10:3 (to disfavor Max/Max dimer formation), and the resulting CD spectra were comparable to the sum of the CD spectra of the individual components. N-myc/MAX bound to 1Ebox DNA with a K_d of ~150 nM, indicating that our samples contained high-quality N-myc/Max dimers. Furthermore, non-canonical E-boxes (NCE) with lower binding affinities towards N-myc (NCE-TC: CATCTG and NCE-TA: CATATG)⁸¹ were used to evaluate the phase separation of N-myc. The N-myc/MAX complex bound to DNA oligomers containing non-canonical E-boxes with K_d values of ~655 and ~735 nM, respectively (Extended Data Fig. 8).

Analytical HPLC approach.

We further quantified effects of Ebox DNA in N-myc/MAX phase separation using an analytical HPLC approach that allowed us to separate the components in the dilute phase and determine the concentration of N-myc⁸², thereby reporting directly on the driving force for phase separation of the system under different conditions. In a buffer without excess salt, N-myc did not undergo phase separation, and we therefore recovered the input concentration (of 25 μM). In a buffer containing 150 mM KCl, the dilute phase concentration of N-myc was ~ 20 μM, reflecting that N-myc molecules in excess of 20 μM concentration were incorporated into condensates. The addition of MAX reduced the dilute phase concentration of N-myc further. While the addition of non-Ebox DNA did not promote stronger phase separation, the successive addition of 1Ebox DNA reduced the N-myc dilute phase concentration further in agreement with our qualitative microscopic results.

Far UV CD spectroscopy.

To confirm refolding, samples were dialyzed in 20 mM phosphate buffer pH 7.5, 50 mM KCl, 10 mM MgCl₂ and 1 mM DTT. The CD spectra were measured for N-myc (10 μM) and Max (3 μM) individually and as a complex in the presence of 1Ebox DNA (50 nM). The spectra were recorded with a J-1500 spectrophotometer (Jasco, USA) at 25 °C. Samples were measured in a 0.1 mm pathlength cuvette (Hellma, Germany). The spectra were accumulated thrice with a response time of 4 s, 1 nm data pitch and 1 nm bandwidth from 195 to 250 nm.

Fluorescence anisotropy binding assay.

A SpectraMax™ fluorescence polarization plate reader was used to assay the binding of Alexa488-labeled DNA oligonucleotide containing 1 Ebox sequence (canonical or non-canonical) to the N-myc (7.5 μM) and Max (2.5 μM) protein mixture (at 3:1 molar ratio) or Max only. The assays were performed using 20 mM HEPES, 150 mM KCl, 10 mM MgCl₂, 1 mM DTT, and 0.01% NP-40 in the non-binding flat bottom 384 well black plate. The concentration of fluorophore-labeled oligonucleotide DNA was fixed at 50 nM. The dissociation constant (K_d) of the interaction between proteins and DNA was estimated by fitting the experimentally acquired polarization values in Origin Pro 8.0⁸³.

Microscopy of N-myc, Max and DNA.

For assessing the driving force for phase separation, samples of N-myc (10 μM), Max (3 μM) and DNA (titration from 0.25 –10 μM for 1Ebox, 3Ebox and 7Ebox, respectively) were incubated in buffer containing 20 mM HEPES pH 7.5, 150 mM KCl, 10 mM MgCl₂ and 1 mM DTT at 25 °C. 4 μL of each sample was sandwiched between an alcohol-cleaned glass slide and coverslip using a 3M 300 LSE high-temperature double-sided tape (0.34 mm) with a cutout window. The microscopy images were captured using a Nikon Eclipse Ni-E Widefield microscope with a 20X objective. For fluorescence imaging, 1% labeled component (LD655-labeled N-myc, Rhodamine red X-labeled Max and Alexa488-labeled DNA oligos) was added to the samples and imaged using the fluorescence Andor camera on the Nikon Eclipse Ni-E Widefield microscope with a 20X objective. For each sample, at least two replicates were imaged.

HPLC phase separation assay.

The N-myc concentration in the dilute phase in the presence of Max and/or DNA oligonucleotides was determined by using analytical HPLC as per the previously established protocol⁸². The input concentration of N-myc was 25 μM for all samples, which were incubated in the presence (or absence) of Max (8 μM) and DNA oligonucleotides (5 μM and 10 μM with 1Ebox or Non-Ebox sequence) in 20 mM HEPES pH 7.5, 150 mM KCl, 10 mM MgCl₂ and 1 mM DTT. N-myc protein without 150 mM KCl was included as a control (which did not phase separate). All solutions were incubated at 25°C for 20 min, then centrifuged for 15 min at 20,000 × g to separate the dilute and dense phases. An equivalent amount of dilute phase was removed from all tubes and diluted as needed by a defined value. The dilute phase solution was then applied to the HPLC C18 (ReproSil Gold 200; Dr. Maisch) reverse-phase column to determine the concentration of N-myc (at 280

nm wavelength). A buffer system with a gradient of H₂O + 0.1% TFA (trifluoroacetic acid, Sigma-Aldrich, USA) with acetonitrile (Alfa Aesar, USA) was used as a solvent system. A standard curve with known concentrations of purified N-myc protein was subjected to HPLC similarly to determine the concentrations of N-myc in the dilute phase for each of the conditions.

Cell proliferation assay.

First, SH-EP cell single clones stably expressing N-myc/SparkDrop or N-myc/SparkDrop control were generated by single-cell dilution and selection after infection of lentivirus containing N-myc/SparkDrop or N-myc/SparkDrop control. Second, cells were grown on clear plastic 96-well plates for 24 hours. Then, the cells were treated with DMSO or lenalidomide (1 μ M; TargetMol, T1642) for 72 hours. CellTiter-Glo reagent (Promega G9243) was added, and the cells were gently shaken for 10 minutes. The mixed content was then moved to white 96-well plates, and luminescence was measured using a Tecan Spark plate reader. For each biological repeat, 6 technical repeats (6 wells) were measured.

RT-qPCR.

2×10^5 of N-myc/SparkDrop and N-myc/SparkDrop control SH-EP stable cells were seeded in 24-well plates. 24 hours after seeding, we added 1 μ M lenalidomide or 0.1% DMSO to the cells (16-hour incubation). We extracted RNA using a Quick-RNA Microprep Kit (Zymo Research, R1051). Complimentary DNA was obtained using a SuperScriptTM IV Reverse Transcriptase (Invitrogen, 18090010). We conducted RT-qPCR on a CFX96 Real-Time PCR. iTaq Universal SYBR Green Supermix was used (Bio-Rad, 1725121) (control: GAPDH). We used these primers:

	Forward primer	Reverse primer	
<i>GAPDH</i>	GTCTCCTCTGACTTCAACAGCG	CTCTTCCTTTGTGCTCTTGCTG	208 bp
<i>SERINC2</i>	GCCTTTGACAACGAGCAGGA	CCAGTTGGTGAGCGTCATCA	102 bp
<i>ANXA8</i>	GGTCACTTGTGCTGTAACCCTG	CCTTGGTTCCTAAGCCCTTCA	250 bp

RNA sequencing and transcriptomic analysis.

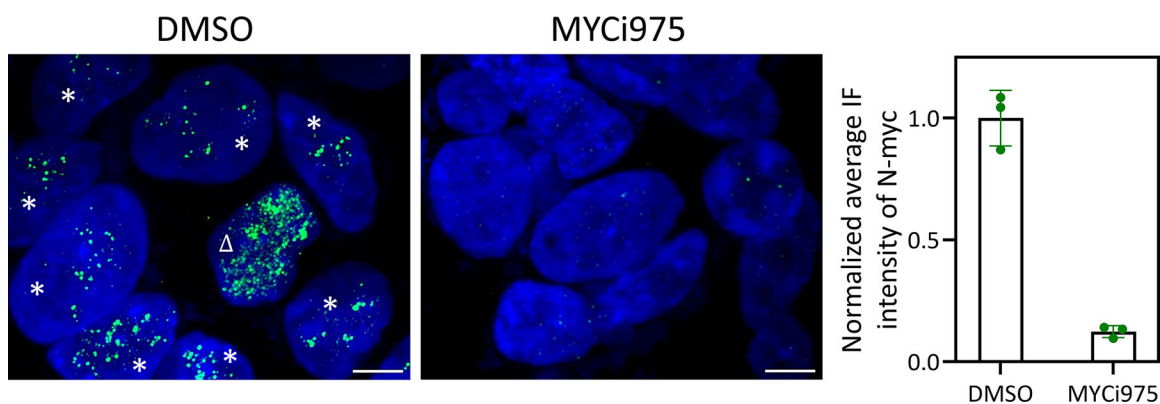
SH-EP cells were infected with lentivirus expressing mEGFP as a baseline sample (without N-myc expression). N-myc/SparkDrop and N-myc/SparkDrop control (no HOTag6) SH-EP stable cells were seeded 1×10^5 cells per cm². 24 hours after seeding, we treated the cells with 1 μ M lenalidomide or 0.1% DMSO for 16 hours. We extracted RNA using a Quick-RNA Microprep Kit (Zymo Reserch, R1051). We constructed the mRNA library, followed by Illumina Novaseq sequencing (Novogene Bioinformatics Technology Co., Ltd). The sequencing generated 20 millions of 150 bp paired-end reads per sample. We first conducted standard Illumina Hiseq demultiplexing. Then we processed the raw data with fastp⁸⁴. We used STAR⁸⁵ to map the reads to the human genome (hg38). We then obtained the raw counts of each gene. We applied edgeR⁸⁶ to the raw counts and identified differentially expressed genes (DEGs). We used TMM normalization and calculated fold change (Log2), P value and false discovery rate (FDR). We plotted volcano plots and visualized DEGs (P

< 0.01, FDR < 0.1). The DEGs of diffuse N-myc (or condensed N-myc) to GFP baseline were determined by $P < 0.01$, $FDR < 0.05$ and $|\log_2FC| > 0.58$. We plotted the gene heatmap by TPM normalization. We performed Gene Ontology (GO) analysis using ClusterProfiler⁸⁶. For principal component analysis (PCA), the raw count matrix was normalized using the DESeq2 default method, and the variance stabilizing transformed data was processed. A screen plot showed that major variance originated from the first component.

Statistics and Reproducibility.

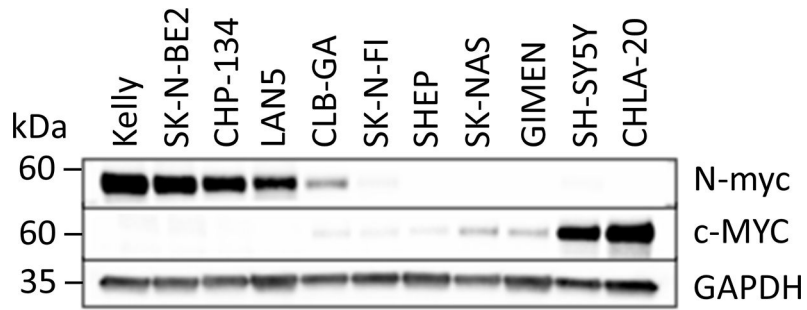
All statistics were performed in GraphPad Prism or Microsoft Excel. Live cell imaging, immunofluorescence staining, in vitro phase separation assays, q-RT-PCR, proliferation assays, and western blots were repeated at least 3 times. RNA-seq was performed in triplicates in one independent experiment for most groups. For MYCN-mEGFP-CEL + DMSO group and MYCN-mEGFP-Cel/iZF-EGFP* + lena group, duplicates in one independent experiment were performed because one replicate failed in the library preparation step. All samples were randomly grouped. Investigators were blinded to group allocation during experiments and not blinded to data analysis. It was impossible to blind the investigators to the experiments as the differences between groups can be easily observed from imaging data.

Extended Data



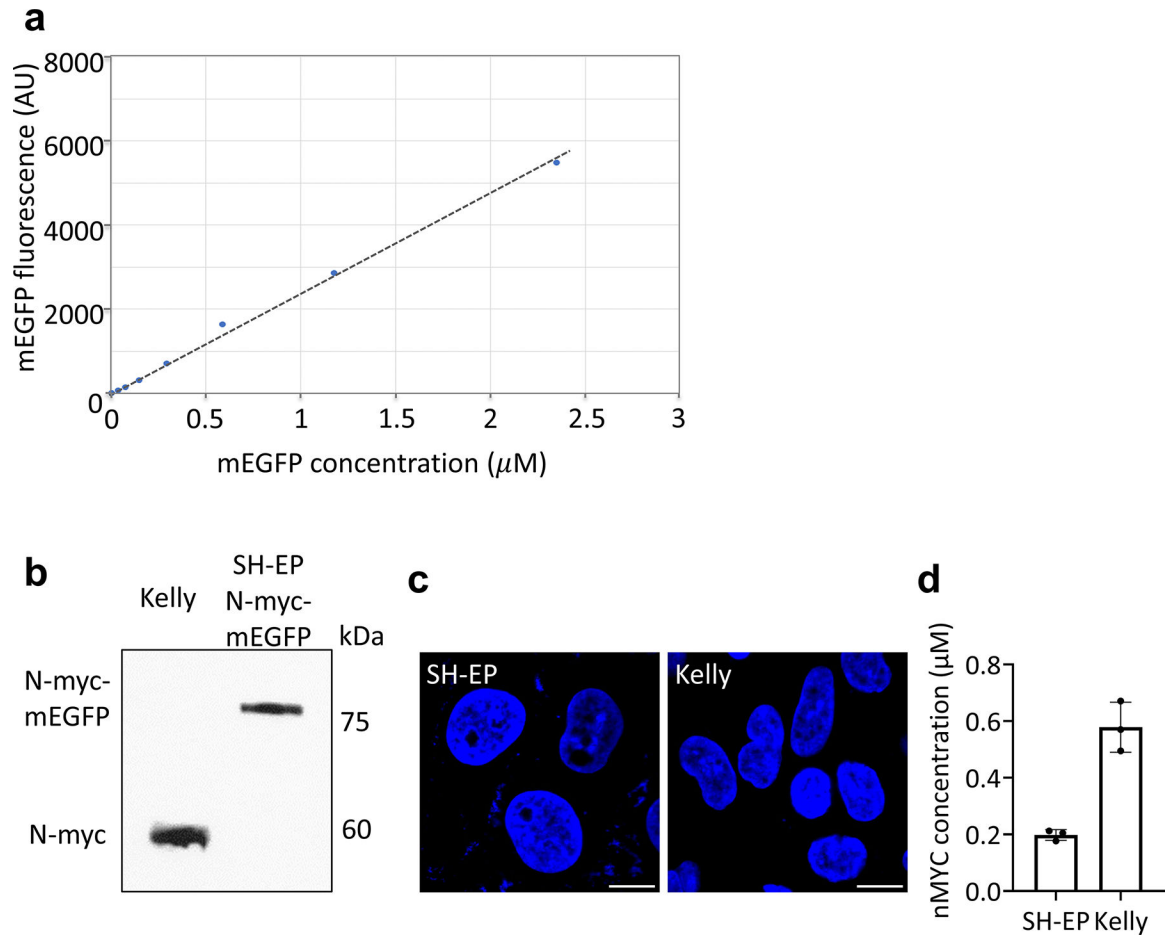
Extended Data Fig. 1 |.

Immunofluorescence images of Kelly cells treated with DMSO or MYC/MAX dimerization inhibitor MYCi975. (Left) Kelly cells were incubated with DMSO or MYCi975 (30 μ M) for 20 hours, followed by immunostaining with N-myc antibody. Stars (*) indicate representative cells. Triangle () indicates few (that is un-representative) cells with high MYCN expression. Scale bar, 5 μ m. (Right) Normalized average N-myc immunofluorescence intensity in DMSO or MYCi975 treated cells. Data are shown as mean \pm SD. N = 3 biological replicates.



Extended Data Fig. 2 |.

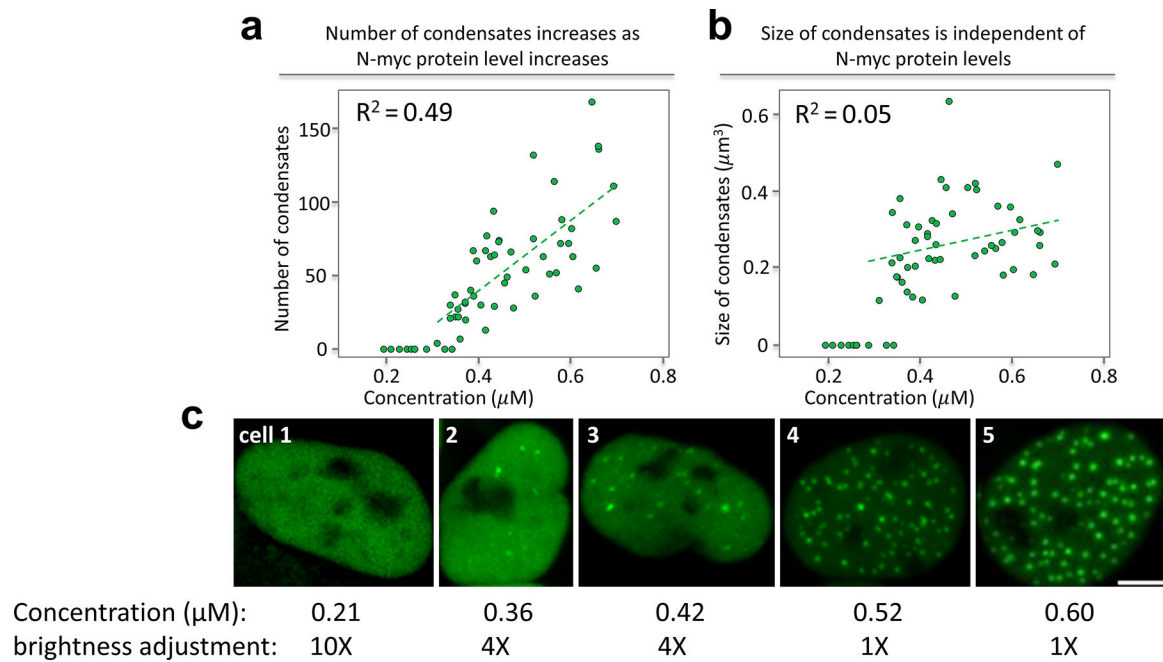
Neuroblastoma cell lines with various degrees of MYC (N-myc, c-MYC) protein expression. Western blot analysis of MYC proteins in various neuroblastoma cells.



Extended Data Fig. 3 |.

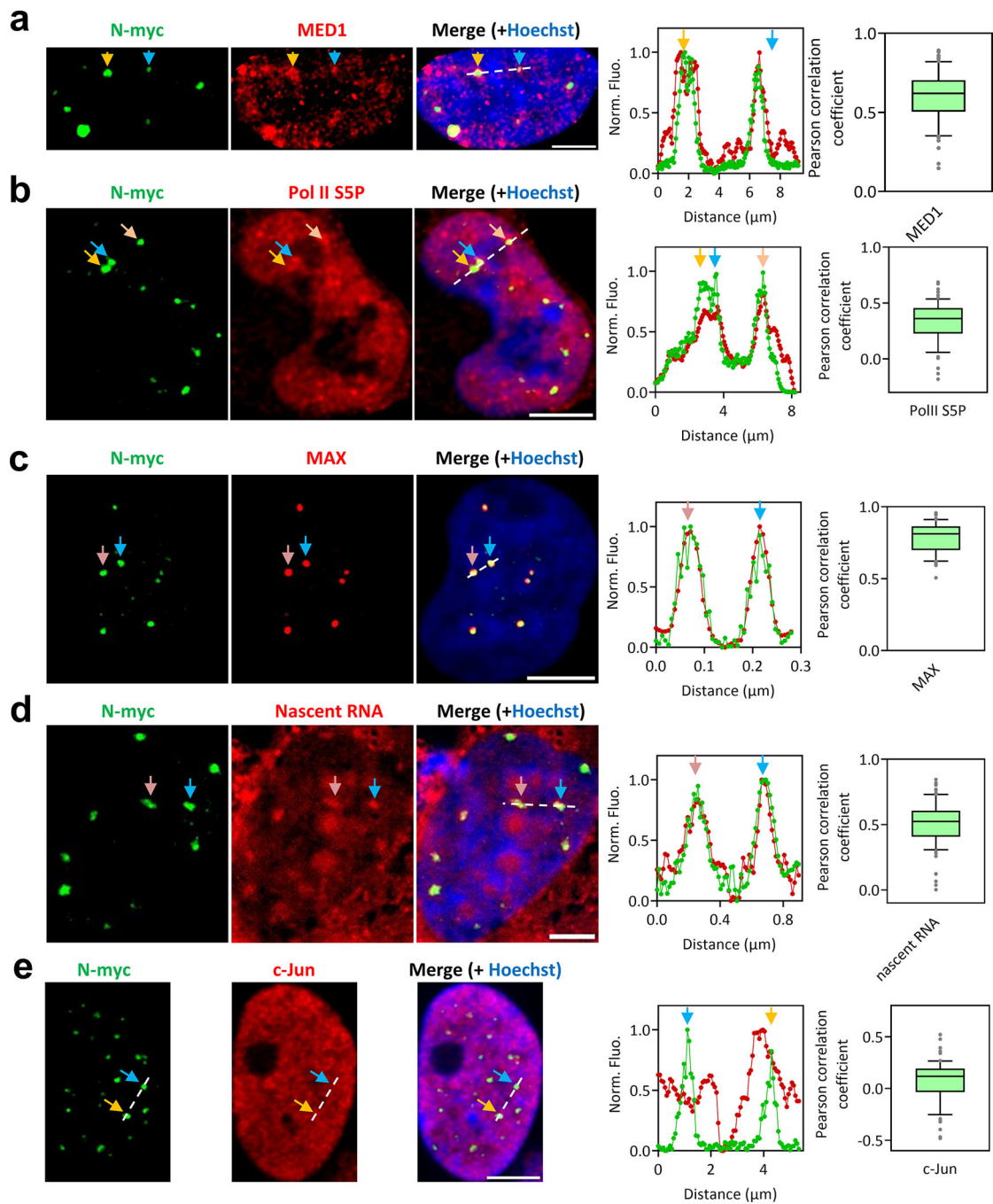
Estimation of N-myc concentration in the Kelly cells. The overall procedure is (a) calculation of an mEGFP concentration-brightness standard curve using purified mEGFP protein. (b) Western blot analysis to determine relative amount of N-myc in Kelly vs SH-EP cells. (c) Fluorescence imaging (Hoechst)-based measurement of the nuclear volume of SH-EP and Kelly cells. The N-myc-mEGFP concentration in SH-EP cells is determined by comparing the fluorescence intensity of N-myc-mEGFP versus that of the purified mEGFP.

(d) Estimation of the N-myc concentration in the nucleus of Kelly cells. Data are mean + SD (n = 20 cells). Scale bar, 10 μm .



Extended Data Fig. 4 |.

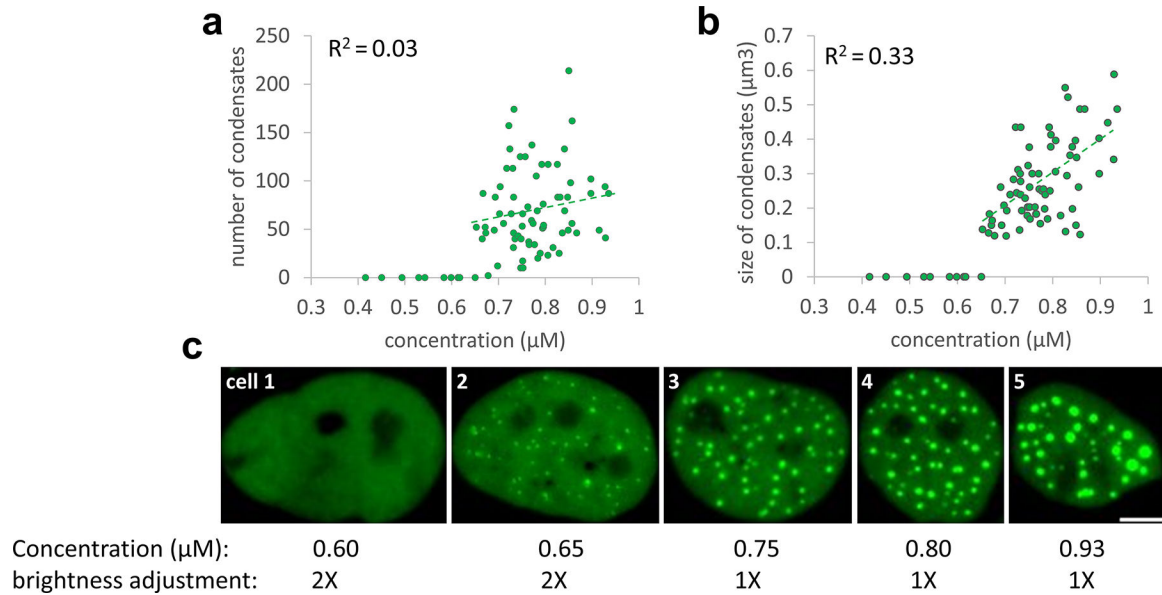
Relationship of N-myc condensate number and size to the N-myc protein levels. (a) Number of N-myc condensates was plotted against the N-myc protein level per nucleus. SH-EP cells expressing N-myc-mEGFP were imaged under the spinning disc confocal microscope. (b) Size of N-myc condensates was plotted against the N-myc protein level in single nucleus. (c) SH-EP cells with different expressing levels of N-myc-mEGFP. Images are max-projected to show all condensates. Dim cells are shown with brightness adjustment as listed. Scale bar: 5 μm .



Extended Data Fig. 5 |

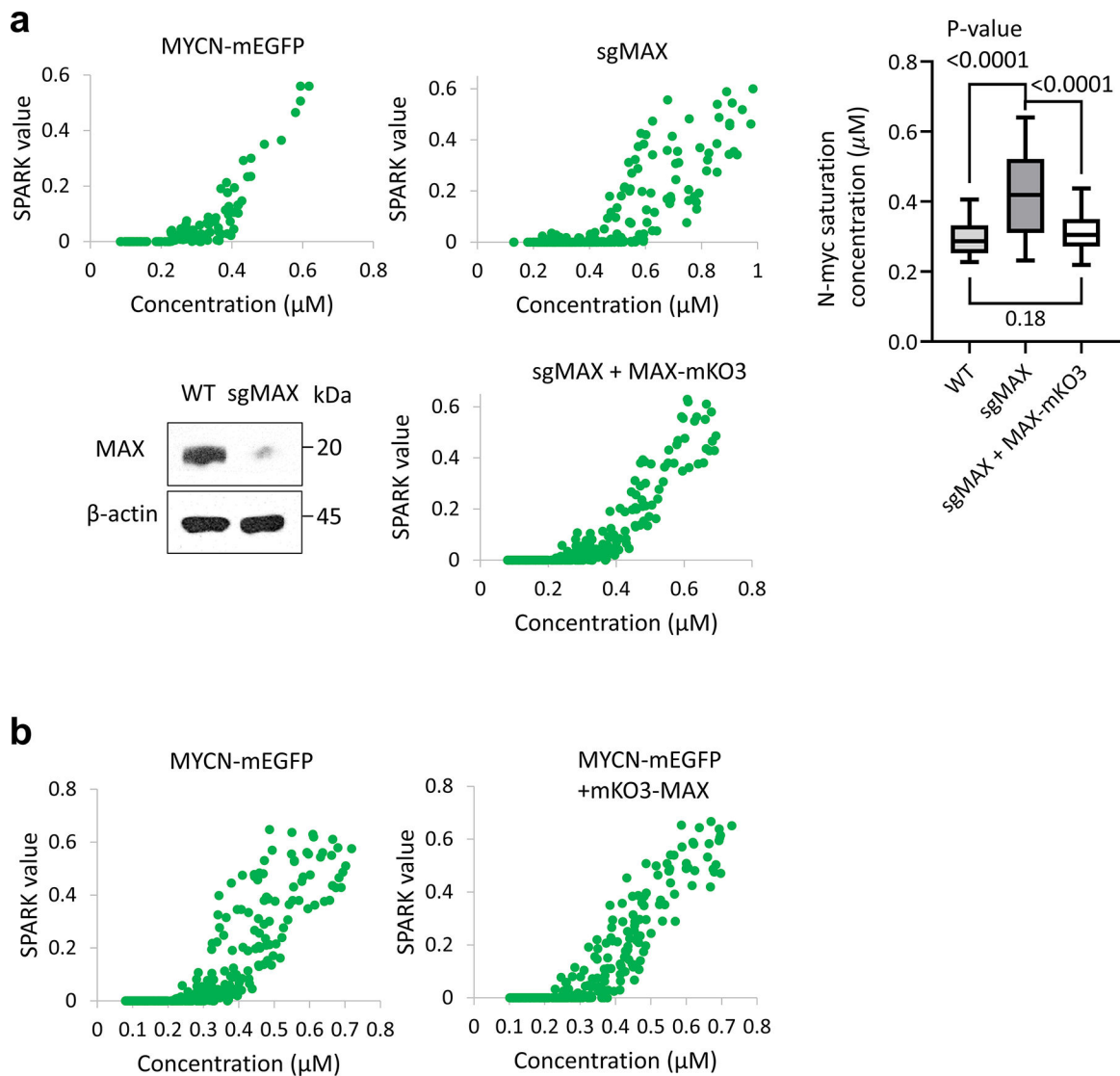
Endogenous N-myc condensates contain DNA-binding and dimerization partner, transcriptional machinery and nascent RNA but do not co-localize with c-Jun. Immunostained N-myc condensates colocalized with MED1 (a), Pol II S5p (b), MAX (c), nascent RNA (d) and c-Jun (e). Kelly cells were stained with antibody against N-myc, and antibodies against MED1, Pol II S5p, or c-Jun, or co-expressed with MAX-mKO3, or labeled by 5-ethynyluridine for labeling nascent RNA. The arrows point to representative condensates. The fluorescence intensity profile (right panel) is extracted from the position

shown by the dashed line. Co-localization assessment by Pearson's correlation coefficient is shown in right panels. Center lines show the median values. Green boxes contain the 25th to 75th percentiles of dataset. Black whiskers mark the 10th and 90th percentiles. Outliers are marked with grey dots. NMED1 = 76, NPol II_{S5P} = 67, NMA_X = 61, Nnascent RNA = 82 cells, Nc_{Jun} = 67 cells. Scale bars, 5 μ m.



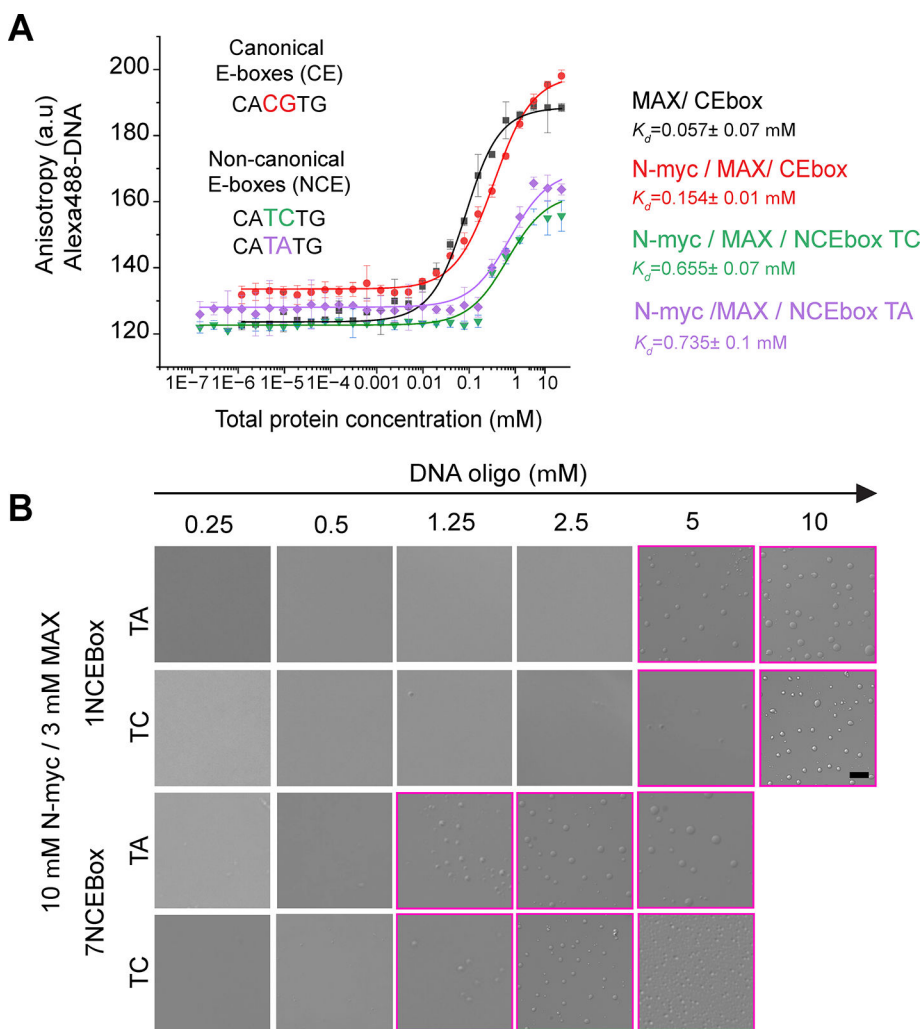
Extended Data Fig. 6 |.

Condensate number and size related to protein levels of the truncated N-myc lacking the DNA-binding domain. (a) Number of N-myc1₋₃₆₅ condensates was plotted against the N-myc protein level per nucleus. (b) Size of N-myc1₋₃₆₅ condensates was plotted against the N-myc protein level in single nucleus. (c) SH-EP cells with different expressing levels of N-myc1₋₃₆₅- mEGFP. Images are max-projected to show all condensates. Dim cells are shown with brightness adjustment as listed. Scale bar: 5 μ m.

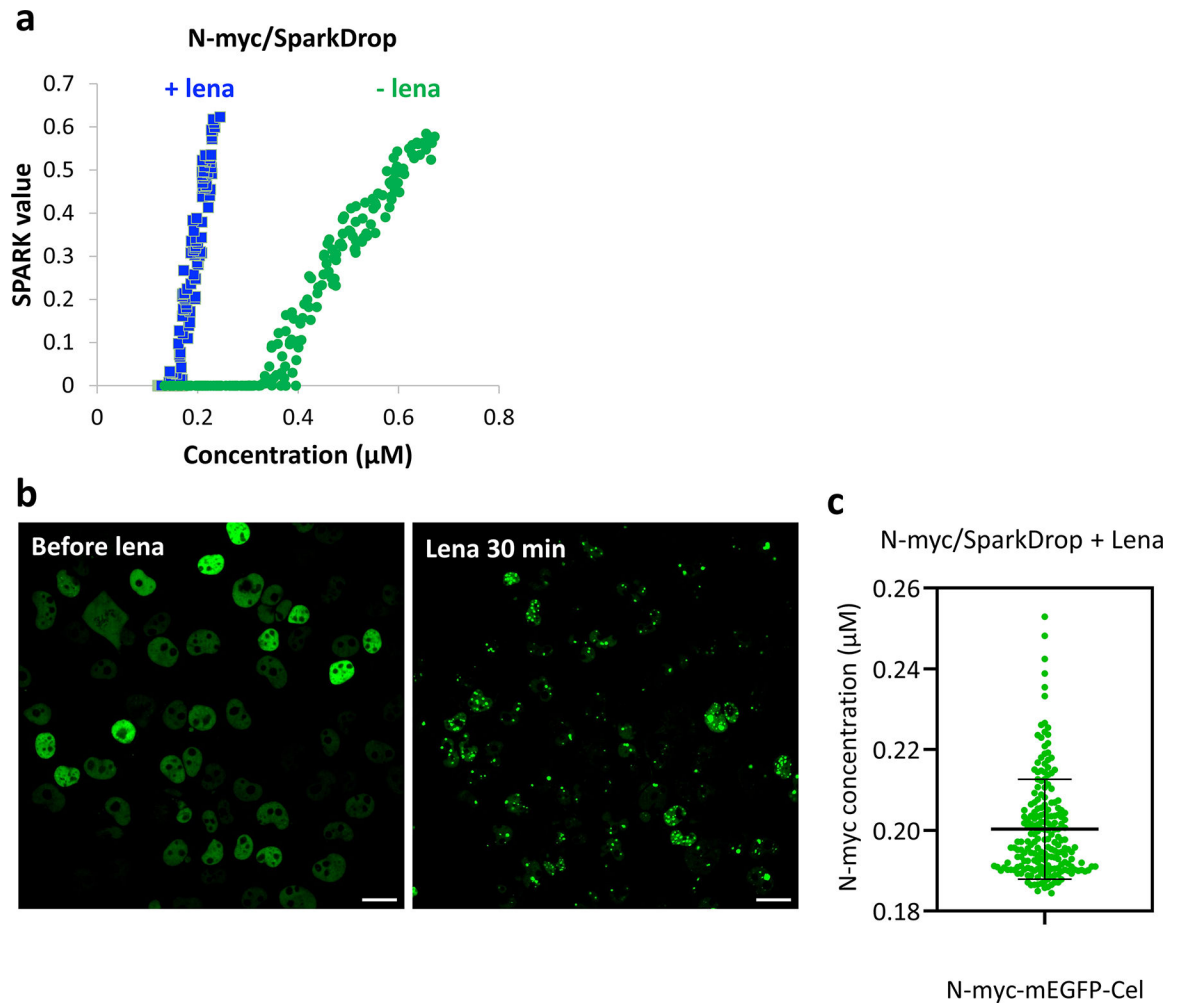


Extended Data Fig. 7 |

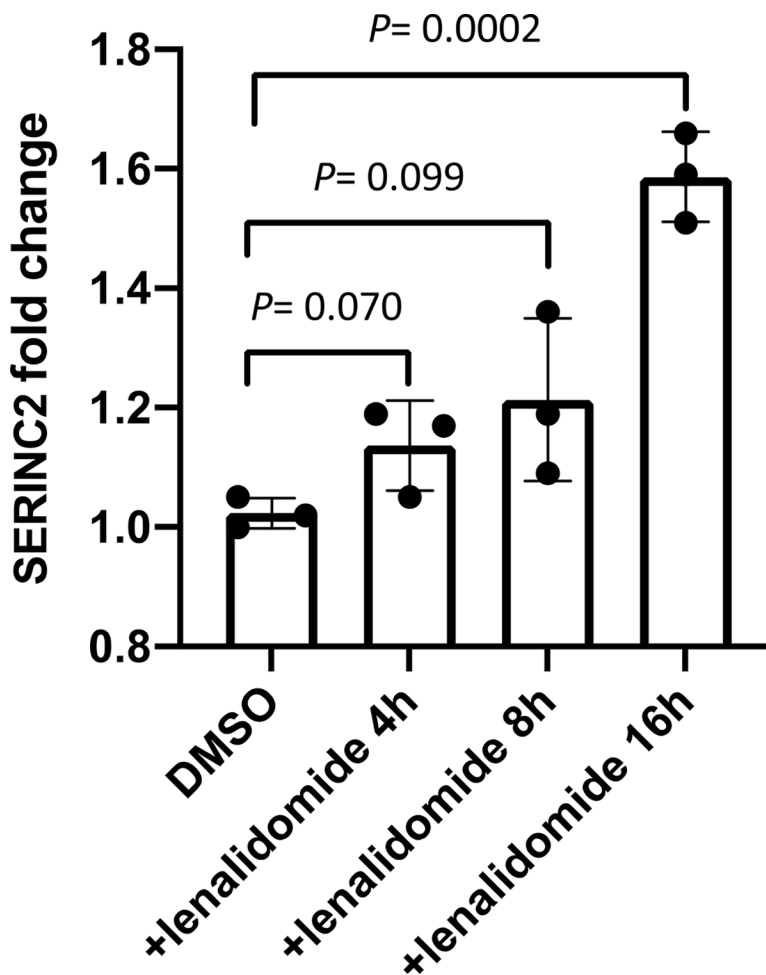
MAX contributes to N-myc phase separation. (a) MAX was knocked out by sgRNA in SH-EP cells expressing MYCN-mEGFP. Top left: SPARK value against N-myc concentration in wild type SH-EP cells expressing MYCN-mEGFP. Top middle: SPARK value against N-myc concentration in MAX-KO SH-EP cells expressing MYCN-mEGFP. Lower left: western blot showing MAX protein level in wild type (WT) and MAX-KO (sgMAX) SH-EP cells. Lower middle: SPARK value in MAX-KO SH-EP cells expressing MYCN-mEGFP and MAX-mKO3. Right panel: N-myc saturation concentration in WT, MAX-KO and rescued SH-EP cells. The MAX-KO SH-EP cells were rescued by expressing MAX-mKO3. Center lines show the median values. Boxes contain the 25th to 75th percentiles of dataset. Whiskers mark the minimum and maximum values. $N_{WT} = 40$, $N_{sgMAX} = 49$, $N_{sgMAX+MAX_mKO3} = 54$. P value, two-sided non-paired t-test. (b) Left: SPARK value against N-myc concentration in SH-EP cells expressing MYCN-mEGFP. Right: SPARK value against N-myc concentration in SH-EP cells expressing MYCN-mEGFP and MAX-mKO3.



Extended Data Fig. 8 |.
Phase separation of full-length N-myc protein is enhanced by DNA oligonucleotides containing non-canonical Myc E-box sequences. (a) Fluorescence anisotropy assay showing binding of the N-Myc / MAX heterodimer to non-canonical E-box DNA in 20 mM HEPES, 150 mM KCl, 10 mM MgCl₂, 1 mM DTT, and 0.01% NP-40 containing buffer. The concentration of fluorophore-labeled oligonucleotide DNA containing 1 NCE-box sequence (CATCTG or CATATG) was fixed at 50 nM and a ratio of Myc / Max of 3:1 was used. The dissociation constant (K_d) of the interaction between proteins and DNA was determined by fitting the experimental data in Origin Pro 8.0 {Roehrl, 2004 #1}. MAX/CEbox and N-myc/MAX/CEbox data are the same as in Fig. 4b. (b) Brightfield microscopy images of solutions containing the N-myc / Max complex (10 .M Myc / 3 .M Max) in the presence of 1NCEbox (26-mer), and 7NCEbox (182 mer) DNA in 20 mM HEPES, 150 mM KCl, 10 mM MgCl₂, 1 mM DTT. Purple boxes highlights the images with N-myc phase separation observed. The images show similar phase separation as with canonical E-box sequences. The scale bar is 5 μ m.

**Extended Data Fig. 9 |**

Saturation concentration of SparkDrop-tagged N-myc and the stable N-myc/SparkDrop SH-EP cells used for the RNAseq experiments. (a) Saturation concentration of SparkDrop-tagged N-myc with and without lenalidomide. Each green dot represents data from a single cell (~200 cells for each group). The concentration was calculated based on the green fluorescence of mEGFP in SparkDrop. (b) Representative images of stable SparkDrop-MYCN cells before and 30 minutes after 1 μM lenalidomide (lена) incubation. Scale bar: 20 μm . (c) N-myc concentration is $0.20 \pm 0.01 \mu\text{M}$ (Mean \pm SD). N = 200 cells.



Extended Data Fig. 10 |.

RT-qPCR of SERINC2 mRNA in SH-EP cells expressing N-myc/SparkDrop treated with 1 μ M lenalidomide for different duration. Data are shown as mean \pm SD. N = 3 biological independent replicates. P value, two-sided non-paired t-test.

Supplementary Material

Refer to Web version on PubMed Central for supplementary material.

Acknowledgments:

We thank Hiten Madhani, Bo Huang, Vijay Ramani, and Eric Holland for critical suggestions. This work was supported by NIH R01CA258237, U01DK127421, R35GM131766 and Benioff Initiative for Prostate Cancer Research Award (to X.S.), and NIH P01CA217959, P30CA082103, U01CA217864, and grants from the Alex Lemonade Stand, St. Baldrick, and Samuel Waxman Cancer Research Foundations (to W.A.W.), U01DA052713 and R21DA056293 (to Y.S.), and ALSAC and the St. Jude Research Collaborative on the Biology and Biophysics of RNP granules (to T.M.). The funders had no role in study design, data collection and analysis, decision to publish or preparation of the manuscript.

Data availability:

The RNAseq raw data were uploaded to GEO database (accession: GSE259300). All other data are available within the text, supplementary information, and source data section.

References

1. Mastop M et al. Characterization of a spectrally diverse set of fluorescent proteins as FRET acceptors for mTurquoise2. *Sci. Rep.* 1–18 (2017). doi:10.1038/s41598-017-12212-x [PubMed: 28127051]
2. Tsutsui H, Karasawa S, Okamura Y & Miyawaki A Improving membrane voltage measurements using FRET with new fluorescent proteins. *Nat Methods* 5, 683–685 (2008). [PubMed: 18622396]
3. Baluapuri A, Wolf E & Eilers M Target gene-independent functions of MYC oncoproteins. *Nat Rev Mol Cell Biol* 1–13 (2020). doi:10.1038/s41580-020-0215-2 [PubMed: 31676888]
4. Dang CV MYC on the Path to Cancer. *Cell* 149, 22–35 (2012). [PubMed: 22464321]
5. Meyer N & Penn LZ Reflecting on 25 years with MYC. *Nat Rev Cancer* 8, 976–990 (2008). [PubMed: 19029958]
6. Carroll PA, Freie BW, Mathsyaraja H & Eisenman RN The MYC transcription factor network: balancing metabolism, proliferation and oncogenesis. *Front. Med* 12, 412–425 (2018). [PubMed: 30054853]
7. Cheng JM et al. Preferential amplification of the paternal allele of the N-myc gene in human neuroblastomas. *Nat Genet* 4, 191–194 (1993). [PubMed: 8102299]
8. Brodeur GM, Seeger RC, Schwab M, Varmus HE & Bishop JM Amplification of N-myc in Untreated Human Neuroblastomas Correlates with Advanced Disease Stage. *Science* 224, 1121–1124 (1984). [PubMed: 6719137]
9. Kohl NE, Gee CE & Alt FW Activated expression of the N-myc gene in human neuroblastomas and related tumors. *Science* 226, 1335–1337 (1984). [PubMed: 6505694]
10. Pugh TJ et al. The genetic landscape of high-risk neuroblastoma. *Nat Genet* 1–9 (2013). doi:10.1038/ng.2529 [PubMed: 23268125]
11. Chantry YH et al. Paracrine signaling through MYCN enhances tumor-vascular interactions in neuroblastoma. *Science Translational Medicine* 4, 115ra3–115ra3 (2012).
12. Murphy DJ et al. Distinct Thresholds Govern Myc’s Biological Output In Vivo. *Cancer Cell* 14, 447–457 (2008). [PubMed: 19061836]
13. Soucek L et al. Modelling Myc inhibition as a cancer therapy. *Nature* 455, 679–683 (2008). [PubMed: 18716624]
14. Smith DP, Bath ML, Metcalf D, Harris AW & Cory S MYC levels govern hematopoietic tumor type and latency in transgenic mice. *Blood* 108, 653–661 (2006). [PubMed: 16537801]
15. Felsher DW & Bishop JM Reversible tumorigenesis by MYC in hematopoietic lineages. *Mol Cell* 4, 199–207 (1999). [PubMed: 10488335]
16. Zeid R et al. Enhancer invasion shapes MYCN-dependent transcriptional amplification in neuroblastoma. *Nat Genet* 1–16 (2018). doi:10.1038/s41588-018-0044-9 [PubMed: 29273803]
17. Choi J-M, Holehouse AS & Pappu RV Physical Principles Underlying the Complex Biology of Intracellular Phase Transitions. *Annual review of biophysics* 49, annurev-biophys-121219-081629–27 (2020).
18. Wheeler RJ & Hyman AA Controlling compartmentalization by non-membrane-bound organelles. *Philosophical Transactions of the Royal Society B: Biological Sciences* 373, 20170193–9 (2018).
19. Banani SF, Lee HO, Hyman AA & Rosen MK Biomolecular condensates: organizers of cellular biochemistry. *Nat Rev Mol Cell Biol* 1–14 (2017). doi:10.1038/nrm.2017.7
20. Hyman AA, Weber CA & Jülicher F Liquid-Liquid Phase Separation in Biology. *Annu Rev Cell Dev Biol* 30, 39–58 (2014). [PubMed: 25288112]
21. Hyman AA & Simons K Cell biology. Beyond oil and water--phase transitions in cells. *Science* 337, 1047–1049 (2012). [PubMed: 22936764]

22. Zamudio AV et al. Mediator Condensates Localize Signaling Factors to Key Cell Identity Genes. *Mol Cell* 1–2 (2019). doi:10.1016/j.molcel.2019.08.016
23. Boija A et al. Transcription Factors Activate Genes through the Phase-Separation Capacity of Their Activation Domains. *Cell* 175, 1842–1855.e16 (2018). [PubMed: 30449618]
24. Chong S et al. Imaging dynamic and selective low-complexity domain interactions that control gene transcription. *Science* 361, eaar2555–11 (2018). [PubMed: 29930090]
25. Hnisz D, Shrinivas K, Young RA, Chakraborty AK & Sharp PA Perspective. *Cell* 169, 13–23 (2017). [PubMed: 28340338]
26. Dekker J et al. Spatial and temporal organization of the genome: Current state and future aims of the 4D nucleome project. *Mol Cell* 1–17 (2023). doi:10.1016/j.molcel.2023.06.018 [PubMed: 36608666]
27. Lyon AS, Peeples WB & Rosen MK A framework for understanding the functions of biomolecular condensates across scales. *Nat Rev Mol Cell Biol* 1–21 (2021). doi:10.1038/s41580-020-00303-z [PubMed: 33244181]
28. Alberti S & Hyman AA Biomolecular condensates at the nexus of cellular stress, protein aggregation disease and ageing. *Nat Rev Mol Cell Biol* 1–18 (2021). doi:10.1038/s41580-020-00326-6 [PubMed: 33244181]
29. Shin Y & Brangwynne CP Liquid phase condensation in cell physiology and disease. *Science* 357, eaaf4382 (2017). [PubMed: 28935776]
30. Li CH et al. MeCP2 links heterochromatin condensates and neurodevelopmental disease. *Nature* 1–28 (2020). doi:10.1038/s41586-020-2574-4
31. Narlikar GJ et al. Is transcriptional regulation just going through a phase? *Mol Cell* 81, 1579–1585 (2021). [PubMed: 33861943]
32. Cai D et al. Phase separation of YAP reorganizes genome topology for long-term YAP target gene expression. *Nat Cell Biol* 1–25 (2019). doi:10.1038/s41556-019-0433-z [PubMed: 30602771]
33. Ahn JH et al. Phase separation drives aberrant chromatin looping and cancer development. *Nature* 1–33 (2021). doi:10.1038/s41586-021-03662-5
34. Tuttle LM et al. Gcn4-Mediator Specificity Is Mediated by a Large and Dynamic Fuzzy Protein-Protein Complex. *CellReports* 22, 3251–3264 (2018).
35. Kar M et al. Phase-separating RNA-binding proteins form heterogeneous distributions of clusters in subsaturated solutions. *Proceedings of the National Academy of Sciences* 119, e2202222119 (2022).
36. Li P et al. Phase transitions in the assembly of multivalent signalling proteins. *Nature* 483, 336–340 (2012). [PubMed: 22398450]
37. Trojanowski J et al. Transcription activation is enhanced by multivalent interactions independent of phase separation. *Mol Cell* 82, 1878–1893.e10 (2022). [PubMed: 35537448]
38. Thody SA et al. Small Molecule Properties Define Partitioning into Biomolecular Condensates. *bioRxiv* 2022.12.19.521099 (2022). doi:10.1101/2022.12.19.521099
39. Klein IA et al. Partitioning of cancer therapeutics in nuclear condensates. *Science* 368, 1386–1392 (2020). [PubMed: 32554597]
40. Kilgore HR et al. Distinct chemical environments in biomolecular condensates. *Nat Chem Biol* 20, 291–301 (2024). [PubMed: 37770698]
41. Chung C-I, Yang J & Shu X Chemogenetic Minitool for Dissecting the Roles of Protein Phase Separation. *ACS Cent. Sci.* 9, 1466–1479 (2023). [PubMed: 37521779]
42. Han H et al. Small-Molecule MYC Inhibitors Suppress Tumor Growth and Enhance Immunotherapy. *Cancer Cell* 1–31 (2019). doi:10.1016/j.ccell.2019.10.001
43. Riback JA et al. Composition-dependent thermodynamics of intracellular phase separation. *Nature* 1–17 (2020). doi:10.1038/s41586-020-2256-2
44. Feric M et al. Coexisting Liquid Phases Underlie Nucleolar Subcompartments. *Cell* 165, 1686–1697 (2016). [PubMed: 27212236]
45. Brangwynne CP, Mitchison TJ & Hyman AA Active liquid-like behavior of nucleoli determines their size and shape in *Xenopus laevis* oocytes. *Proceedings of the National Academy of Sciences* 108, 4334–4339 (2011).

46. Malhis N, Jacobson M & Gsponer J MoRFchibi SYSTEM: software tools for the identification of MoRFs in protein sequences. *Nucleic Acids Res* 44, W488–93 (2016). [PubMed: 27174932]
47. Andresen C et al. Transient structure and dynamics in the disordered c-Myc transactivation domain affect Bin1 binding. *Nucleic Acids Res* 40, 6353–6366 (2012). [PubMed: 22457068]
48. McEwan IJ, Dahlman-Wright K, Ford J & Wright AP Functional interaction of the c-Myc transactivation domain with the TATA binding protein: evidence for an induced fit model of transactivation domain folding. *Biochemistry* 35, 9584–9593 (1996). [PubMed: 8755740]
49. Chen L et al. p53 is a direct transcriptional target of MYCN in neuroblastoma. *Cancer Res* 70, 1377–1388 (2010). [PubMed: 20145147]
50. Reisman D, Elkind NB, Roy B, Beamon J & Rotter V c-Myc trans-activates the p53 promoter through a required downstream CACGTG motif. *Cell Growth Differ* 4, 57–65 (1993). [PubMed: 8494784]
51. Sabari BR et al. Coactivator condensation at super-enhancers links phase separation and gene control. *Science* 361, eaar3958–13 (2018). [PubMed: 29930091]
52. Rai AK, Chen J-X, Selbach M & Pelkmans L Kinase-controlled phase transition of membraneless organelles in mitosis. *Nature* 1–25 (2018). doi:10.1038/s41586-018-0279-8
53. Spencer CA, Kruhlak MJ, Jenkins HL, Sun X & Bazett-Jones DP Mitotic Transcription Repression in Vivo in the Absence of Nucleosomal Chromatin Condensation. *J Cell Biol* 150, 13–26 (2000). [PubMed: 10893252]
54. Gottesfeld JM & Forbes DJ Mitotic repression of the transcriptional machinery. *Trends Biochem Sci* 22, 197–202 (1997). [PubMed: 9204705]
55. Yu D et al. a naturally monomeric infrared fluorescent protein for protein labeling. *Nat Methods* 12, 763–765 (2015). [PubMed: 26098020]
56. Shu X Imaging dynamic cell signaling in vivo with new classes of fluorescent reporters. *Current opinion in chemical biology* 54, 1–9 (2020). [PubMed: 31678813]
57. Vagnarelli P Mitotic chromosome condensation in vertebrates. *Exp Cell Res* 318, 1435–1441 (2012). [PubMed: 22475678]
58. Nair SK & Burley SK X-ray structures of Myc-Max and Mad-Max recognizing DNA. Molecular bases of regulation by proto-oncogenic transcription factors. *Cell* 112, 193–205 (2003). [PubMed: 12553908]
59. Morin JA et al. Sequence-dependent surface condensation of a pioneer transcription factor on DNA. *Nature physics* 18, 271–276 (2022).
60. Zhang Q et al. Visualizing Dynamics of Cell Signaling In Vivo with a Phase Separation-Based Kinase Reporter. *Mol Cell* 69, 334–345.e5 (2018). [PubMed: 29307513]
61. Chung C-I, Zhang Q & ORCID: 0000-0001-9248-7095, X. S. Dynamic Imaging of Small Molecule Induced Protein-Protein Interactions in Living Cells with a Fluorophore Phase Transition Based Approach. *Anal Chem* 1–7 (2018). doi:10.1021/acs.analchem.8b03476 [PubMed: 29291620]
62. Jiang X et al. Annexin A8 (ANXA8) regulates proliferation of porcine endometrial cells via Akt signalling pathway. *Reprod Domest Anim* 54, 3–10 (2019).
63. Zeng Y et al. SERINC2-knockdown inhibits proliferation, migration and invasion in lung adenocarcinoma. *Oncol Lett* 16, 5916–5922 (2018). [PubMed: 30405754]
64. Zeller KI, Jegga AG, Aronow BJ, O'Donnell KA & Dang CV An integrated database of genes responsive to the Myc oncogenic transcription factor: identification of direct genomic targets. *Genome Biol.* 4, R69–10 (2003). [PubMed: 14519204]
65. Sabò A et al. Selective transcriptional regulation by Myc in cellular growth control and lymphomagenesis. *Nature* 511, 488–492 (2014). [PubMed: 25043028]
66. Walz S et al. Activation and repression by oncogenic MYC shape tumour-specific gene expression profiles. *Nature* 1–18 (2014). doi:10.1038/nature13473
67. Zenk F et al. HP1 drives de novo 3D genome reorganization in early Drosophila embryos. *Nature* 1–27 (2021). doi:10.1038/s41586-021-03460-z
68. Chandra B et al. Phase Separation Mediates NUP98 Fusion Oncoprotein Leukemic Transformation. *Cancer Discovery* 12, 1152–1169 (2022). [PubMed: 34903620]

69. Shi B et al. UTX condensation underlies its tumour-suppressive activity. *Nature* 1–40 (2021). doi:10.1038/s41586-021-03903-7
70. Peebles W & Rosen MK Mechanistic dissection of increased enzymatic rate in a phase-separated compartment. *Nat Chem Biol* 1–18 (2021). doi:10.1038/s41589-021-00801-x [PubMed: 33328655]
71. Case LB, Zhang X, Ditlev JA & Rosen MK Stoichiometry controls activity of phase-separated clusters of actin signaling proteins. *Science* 363, 1093–1097 (2019). [PubMed: 30846599]
72. Huang WYC et al. A molecular assembly phase transition and kinetic proofreading modulate Ras activation by SOS. *Science* 363, 1098– (2019). [PubMed: 30846600]
73. Riback JA et al. Stress-Triggered Phase Separation Is an Adaptive, Evolutionarily Tuned Response. *Cell* 168, 1028–1040.e19 (2017). [PubMed: 28283059]
74. Mittag T & Pappu RV A conceptual framework for understanding phase separation and addressing open questions and challenges. *Mol Cell* 82, 2201–2214 (2022). [PubMed: 35675815]
75. Chung C-I et al. Phase separation of YAP-MAML2 differentially regulates the transcriptome. *Proceedings of the National Academy of Sciences* 121, e2310430121 (2024).

Methods-only Reference

78. Jao CY & Salic A Exploring RNA transcription and turnover in vivo by using click chemistry. *Proceedings of the National Academy of Sciences* 105, 15779–15784 (2008).
79. Pillai-Kastoori L, Schutz-Geschwender AR & Harford JA A systematic approach to quantitative Western blot analysis. *Analytical Biochemistry* 593, 113608 (2020). [PubMed: 32007473]
80. Farina A, Faiola F & Martinez E Reconstitution of an E box-binding Myc:Max complex with recombinant full-length proteins expressed in *Escherichia coli*. *Protein Expr Purif* 34, 215–222 (2004). [PubMed: 15003254]
81. Zeid R et al. Enhancer invasion shapes MYCN-dependent transcriptional amplification in neuroblastoma. *Nat Genet* 1–16 (2018). doi:10.1038/s41588-018-0044-9 [PubMed: 29273803]
82. Bremer A et al. Quantifying Coexistence Concentrations in Multi-Component Phase-Separating Systems Using Analytical HPLC. *Biomolecules* 12, 1480 (2022). [PubMed: 36291688]
83. Roehrl MHA, Wang JY & Wagner G A general framework for development and data analysis of competitive high-throughput screens for small-molecule inhibitors of protein-protein interactions by fluorescence polarization. *Biochemistry* 43, 16056–16066 (2004). [PubMed: 15610000]
84. Chen S, Zhou Y, Chen Y & Gu J fastp: an ultra-fast all-in-one FASTQ preprocessor. *Bioinformatics* 34, i884–i890 (2018). [PubMed: 30423086]
85. Dobin A et al. STAR: ultrafast universal RNA-seq aligner. *Bioinformatics* 29, 15–21 (2013). [PubMed: 23104886]
86. Robinson MD, McCarthy DJ & Smyth GK edgeR: a Bioconductor package for differential expression analysis of digital gene expression data. *Bioinformatics* 26, 139–140 (2010). [PubMed: 19910308]

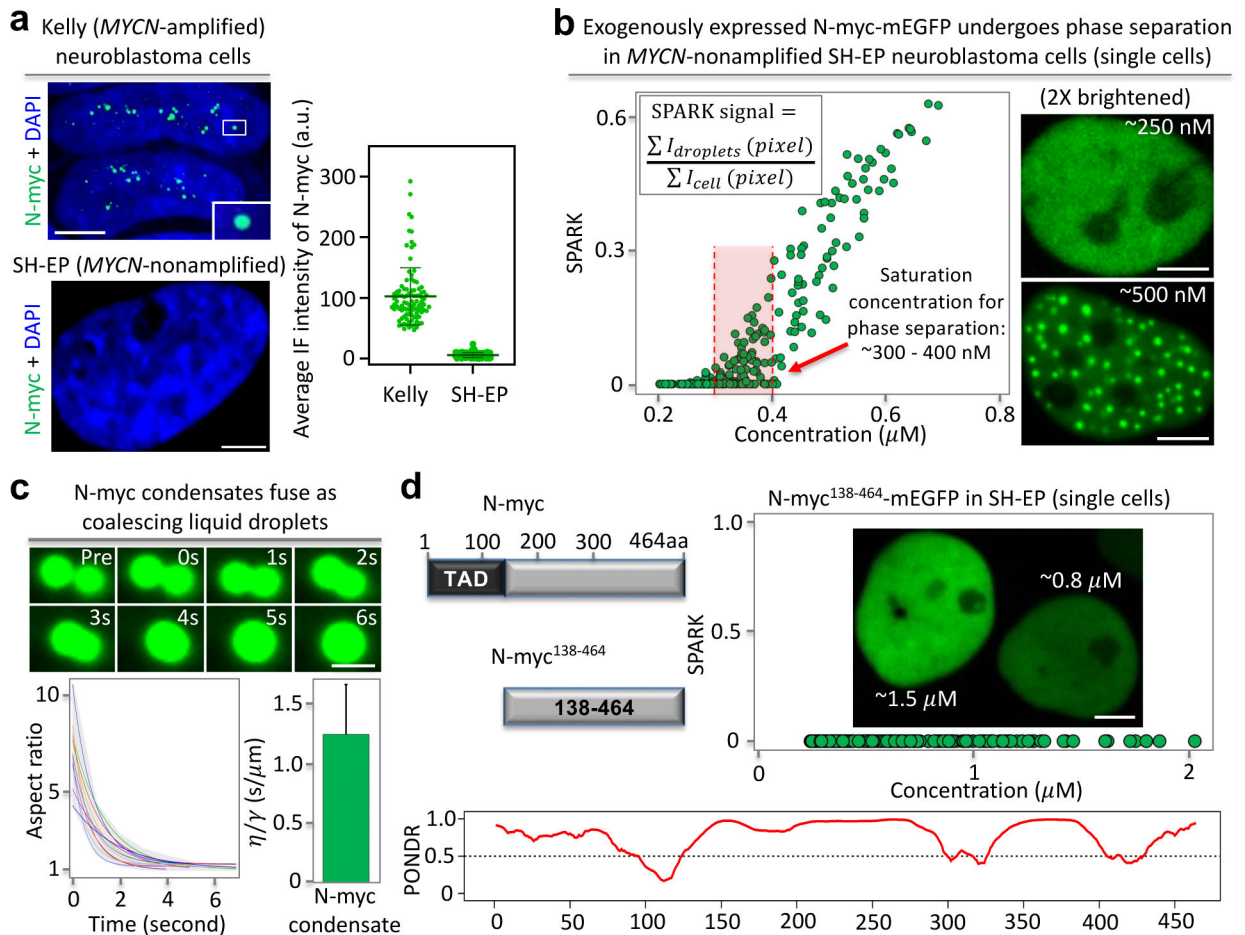


Fig. 1. N-myc undergoes phase separation, which requires the intrinsically disordered transactivation domain.

(a) Immunofluorescence images of N-myc in *MYCN*-amplified neuroblastoma Kelly cells (top left panel) and the *MYCN*-nonamplified SH-EP cells (bottom left panel). N-myc forms puncta in the Kelly cells but not in the SH-EP cells that express no or little N-myc (Fig. S3). Right panel, average N-myc antibody fluorescence intensity in Kelly and SH-EP cells ($N \sim 100$ cells from 3 biological replicates). Data are shown as mean \pm SD. Each dot represents one cell. Scale bar, 10 μm . (b) Expression of mEGFP fused N-myc in the neuroblastoma SH-EP cells that have no or little endogenous N-myc protein expression. Left: quantitative analysis of N-myc puncta formation against its protein level in single cells. Each green circle corresponds to an individual cell, i.e. ~ 300 cells were analyzed. The concentration of the fusion protein was estimated based on purified mEGFP (see details in Methods). The red dashed lines depict a range of saturation concentrations for phase separation. Right: representative fluorescence images; the upper panel is brightened, the lower is not. Scale bar, 5 μm . (c) Coalescence events between N-myc condensates. Top: time-lapse fluorescence images. Scale bar, 1 μm . Bottom-left: Aspect ratio over time. Quantitative analysis of the coalescence events was plotted. Each line represents the best fit for each event. Gray shade indicates the range. Bottom-right: inverse capillary velocity derived from coalescence events. Data are shown as mean+SD ($n = 12$). (d) Quantitative analysis of the truncated N-myc lacking N-terminal TAD, which is an IDR. Each green circle corresponds to an

individual cell (~200 cells). Disorder prediction by PONDR is shown at the bottom. Scale bar, 5 μm .

Author Manuscript

Author Manuscript

Author Manuscript

Author Manuscript

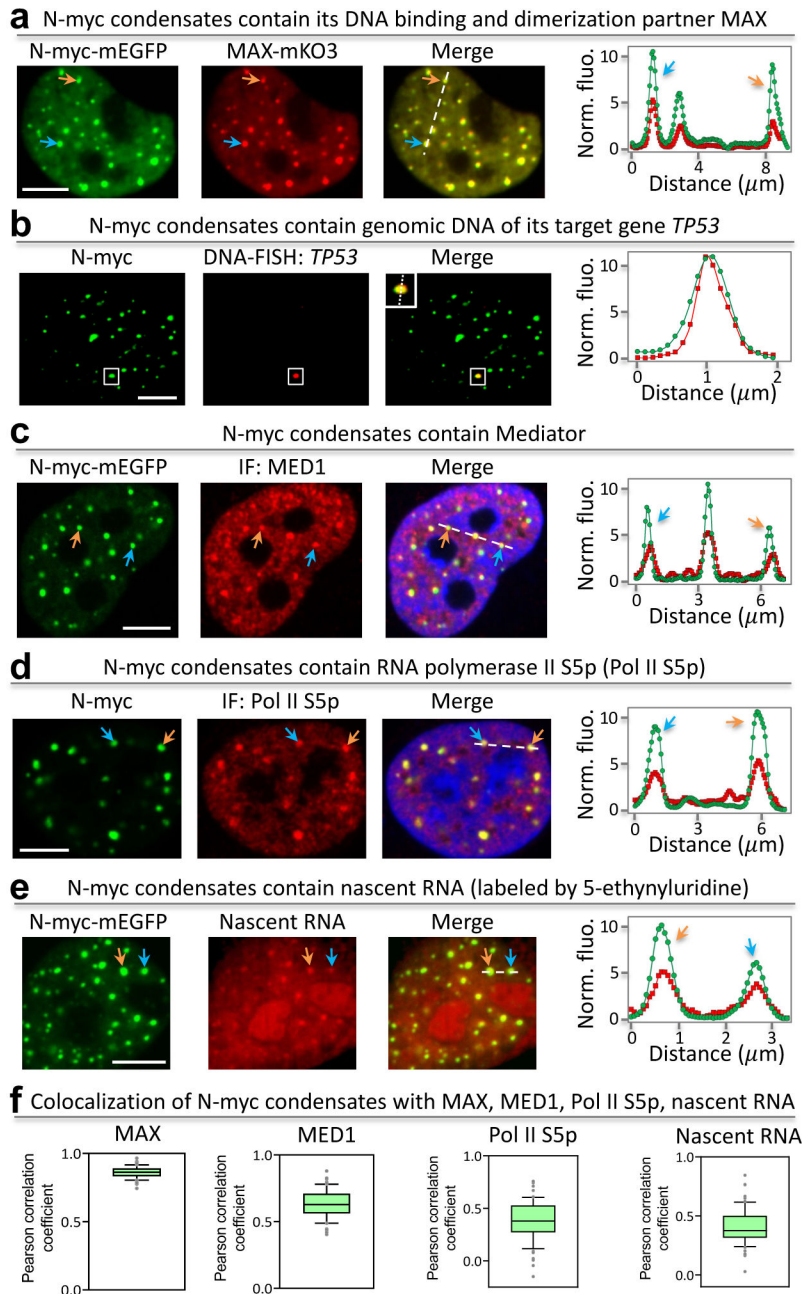


Fig. 2. N-myc condensates contain transcriptional markers including DNA-binding and dimerization partner, genomic DNA, transcriptional machinery and nascent RNA. (a) Fluorescence images of N-myc-mEGFP and MAX-mKO3 in SH-EP cells. Representative condensates are indicated by arrows. (b) Fluorescence images of N-myc condensates with single molecule DNA FISH against *TP53*. (c) Immunofluorescence (IF) images of MED1 with N-myc-mEGFP condensates. (d) IF-imaged Pol II S5p with fluorescence images of N-myc-mEGFP. (e) 5-ethynyluridine-labeled nascent RNA with fluorescence images of N-myc-mEGFP condensates. (f) Co-localization assessment by Pearson’s correlation coefficient. Center lines show the median values. Green boxes contain the 25th to 75th percentiles of dataset. Black whiskers mark the 10th and 90th percentiles.

Outliers are marked with grey dots. Data are mean \pm SD. The profile of fluorescence intensity corresponds to the position indicated by the dashed line. Arrows in the profile plot point to the condensates with colocalization. NMAX = 63, NMED1 = 70, NPol II-S5P = 63, Nnascent RNA = 67 cells. Scale bars, 5 μ m (a – e).

Author Manuscript

Author Manuscript

Author Manuscript

Author Manuscript

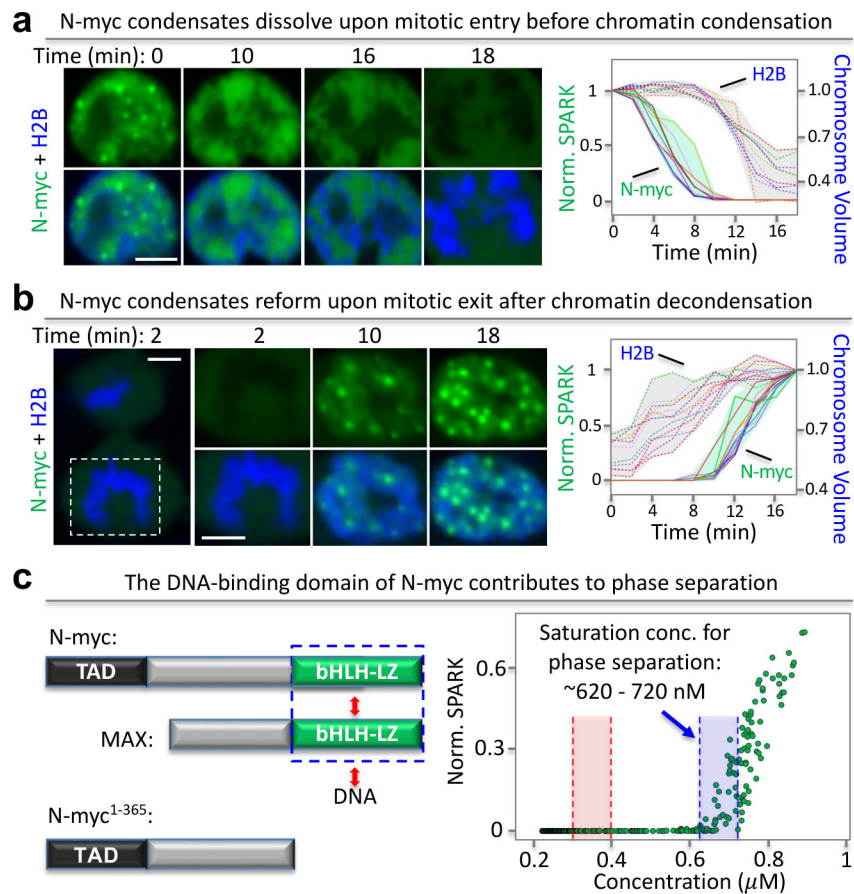


Fig. 3. Disassembly and assembly of N-myc condensates during mitotic entry and exit, respectively.

(a) Time-lapse fluorescence images of SH-EP cells expressing N-myc-mEGFP when cells enter mitosis. mIFP-tagged histone 2B (H2B, in blue) was co-expressed and used to calculate the chromosome volume. Right panel: plots of quantitatively analyzed condensate dissolution and chromosome condensation over time. Each line indicates a single-cell trace ($n = 11$ cells). Shades show the maximum and minimum values of data. (b) Time-lapse fluorescence images of SH-EP cells expressing N-myc-mEGFP when cells exit mitosis. Right panel: plots of quantitatively analyzed reformation of N-myc condensates and chromosome de-condensation. Each line indicates a single-cell trace ($n = 12$ cells). Shades show the maximum and minimum values of data. (c) Expression of the truncated N-myc lacking the DNA-binding domain in SH-EP cells. The blue box depicts a range of saturation concentrations for N-myc¹⁻³⁶⁵ phase separation. The red box depicts a range of saturation concentrations for full length N-myc phase separation (see Fig. 1b). Scale bars, 5 μm (a, b).

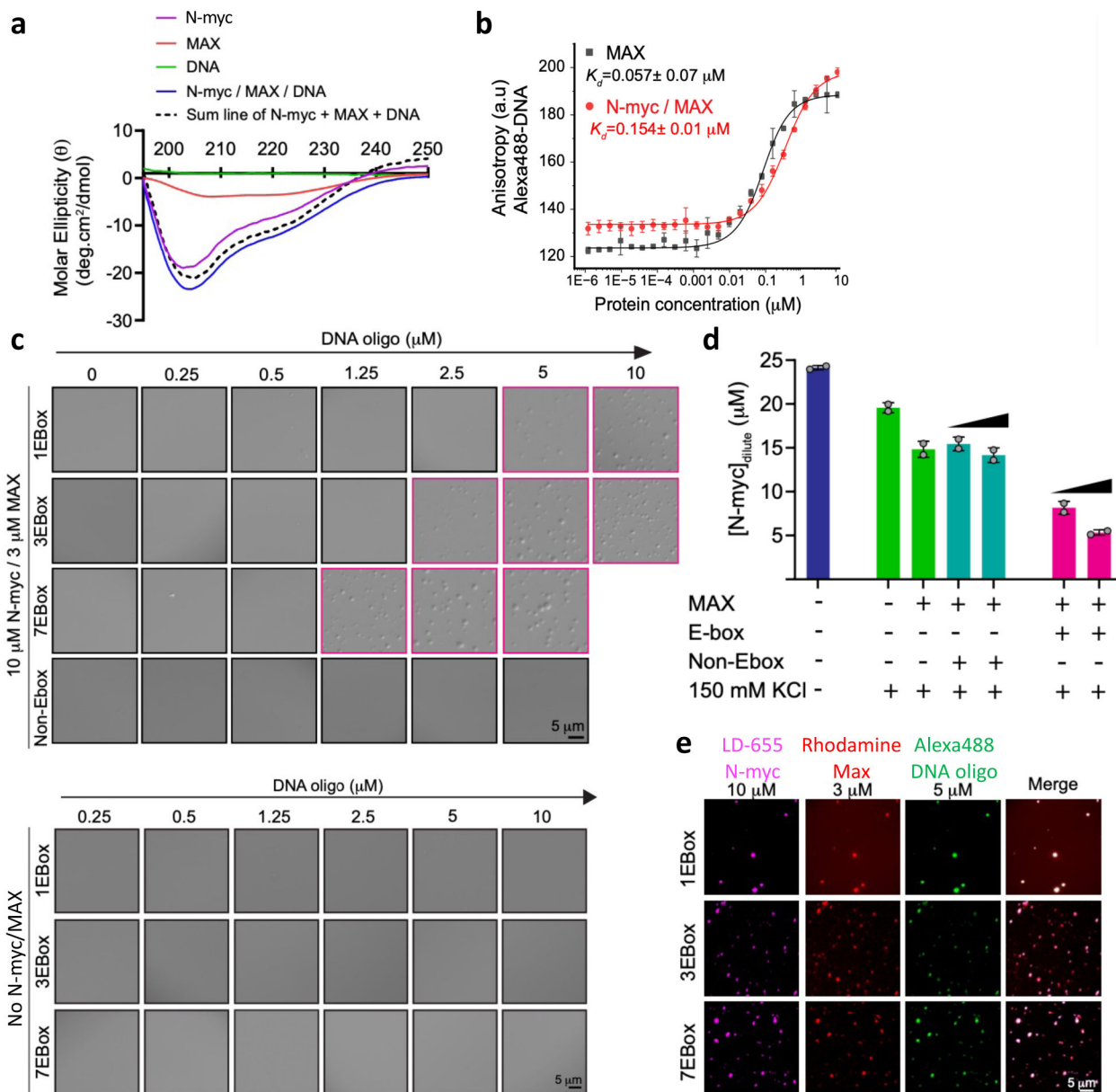


Fig. 4. Phase separation of full-length N-myc protein is enhanced by Max and DNA oligonucleotides containing Myc E-box sequences.
(a) Far UV circular dichroism (CD) spectra for N-myc, MAX, oligonucleotide DNA containing 1 E-box sequence (CACGTG, referred to as 1EBox DNA) and for a complex of all three. The sum of the individual spectra is shown for comparison. The minima at 208 and 222 nm indicate helical structure. **(b)** Fluorescence anisotropy assay showing binding of the N-Myc / MAX heterodimer to 50 nM fluorophore-labeled 1Ebox DNA. The ratio of Myc / Max was fixed at 3:1. The data are the mean of 3 replicates, the error bars \pm SD. **(c)** Differential Interference Contrast (DIC) microscopy images of N-myc / Max complex (10 μM Myc / 3 μM Max) in presence of 1Ebox (26-mer), 3Ebox (78-mer) and 7Ebox (182 mer) DNA. Purple boxes highlights the images with N-myc phase separation observed. Non-Ebox DNA (with sequence TTAGCA instead of the E-box; 182-mer) did not induce any phase

separation under the concentrations evaluated. Solution conditions were 20 mM HEPES, 150 mM KCl, 10 mM MgCl₂, 1 mM DTT. **(d)** Quantification of dilute phase concentration of 25 μM N-myc by analytical HPLC. No phase separation was seen without 150 mM KCl (blue bar). N-myc phase separation is progressively enhanced by Max and the further addition of 1Ebox DNA (at 5 and 10 μM; green and magenta bars, respectively). Non-Ebox DNA (at 5 and 10 μM; cyan bars) did not change the N-myc dilute phase concentration and therefore did not cause phase separation. Data are mean ± SD (n = 2 samples). **(e)** Phase-separated condensates contain N-myc, Max and DNA oligonucleotides as evidenced by fluorescence imaging of LD-655-labeled N-myc, Rhodamine Red X-labeled Max and Alexa 488-labeled DNA oligonucleotides. **(f)** DIC images of 1Ebox, 3Ebox and 7Ebox DNA only (without N-myc and Max proteins), which did not phase separate. Solution conditions were 20 mM HEPES, 150 mM KCl, 10 mM MgCl₂, 1 mM DTT.

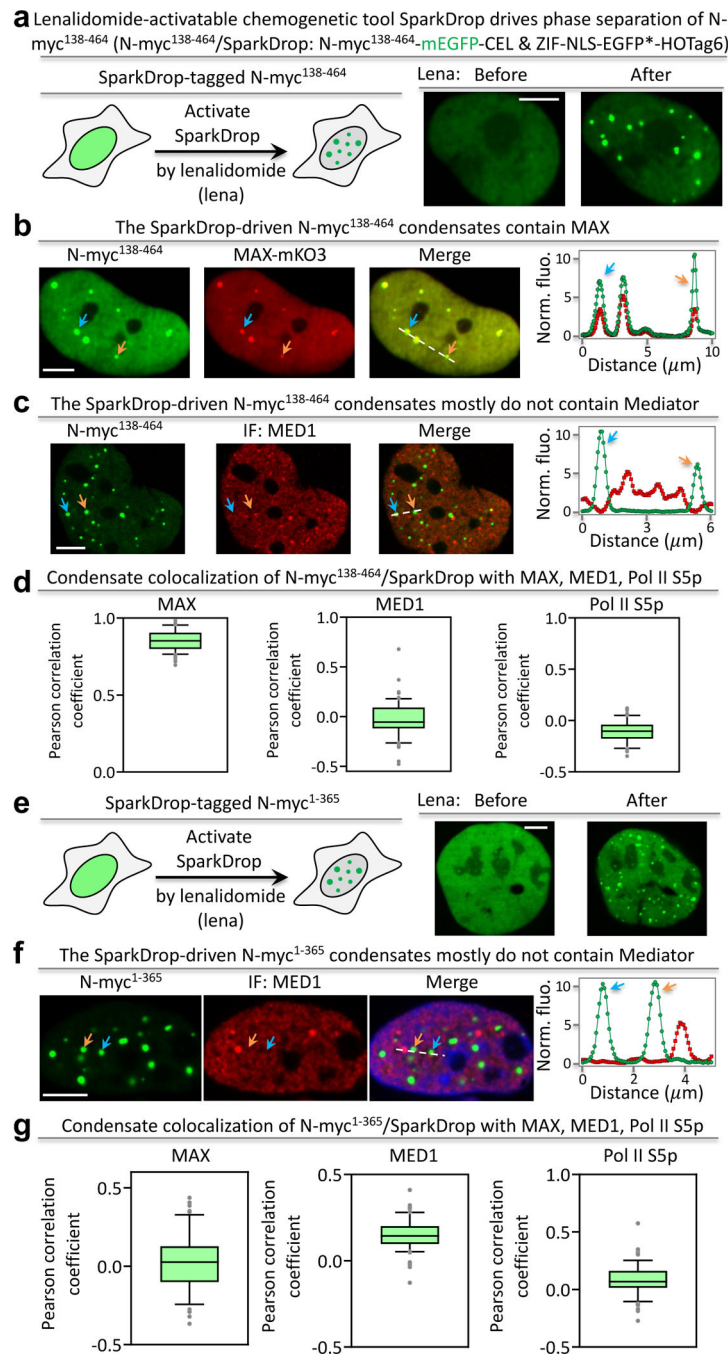


Fig. 5. th TAD and DNA-binding domain are required for transcriptional activity of N-myc condensates.

Bo (a) Lenalidomide-activatable SparkDrop drives phase separation of a truncated N-myc lacking TAD. (b-c) Fluorescence images of N-myc¹³⁸⁻⁴⁶⁴/SparkDrop with MAX-mKO3 (b) and MED1 (c). The profile of fluorescence intensity corresponds to the position indicated by the dashed line. Arrows in the profile plot point to the condensates with colocalization. (d) Co-localization assessment by Pearson's correlation coefficient. Center lines show the median values. Green boxes contain the 25th to 75th percentiles of dataset. Black

whiskers mark the 10th and 90th percentiles. Outliers are marked with grey dots. $N_{MAX} = 71$, $N_{MED1} = 68$, $N_{Pol II-S5P} = 67$. Data are mean \pm SD. **(e)** Lenalidomide-activatable SparkDrop drives phase separation of a truncated N-myc lacking DNA-binding domain. **(f)** Fluorescence images showing SparkDrop-driven N-myc¹⁻³⁶⁵ condensates do not colocalize with MED1. The profile of fluorescence intensity corresponds to the position indicated by the dashed line. Arrows in the profile plot point to the condensates with colocalization. **(g)** Co-localization assessment by Pearson's correlation coefficient. Data are mean \pm SD. $N_{MAX} = 68$, $N_{MED1} = 64$, $N_{Pol II-S5P} = 65$ cells. Center lines show the median values. Green boxes contain the 25th to 75th percentiles of dataset. Black whiskers mark the 10th and 90th percentiles. Outliers are marked with grey dots. Scale bars: 5 μ m (a – c, e, f).

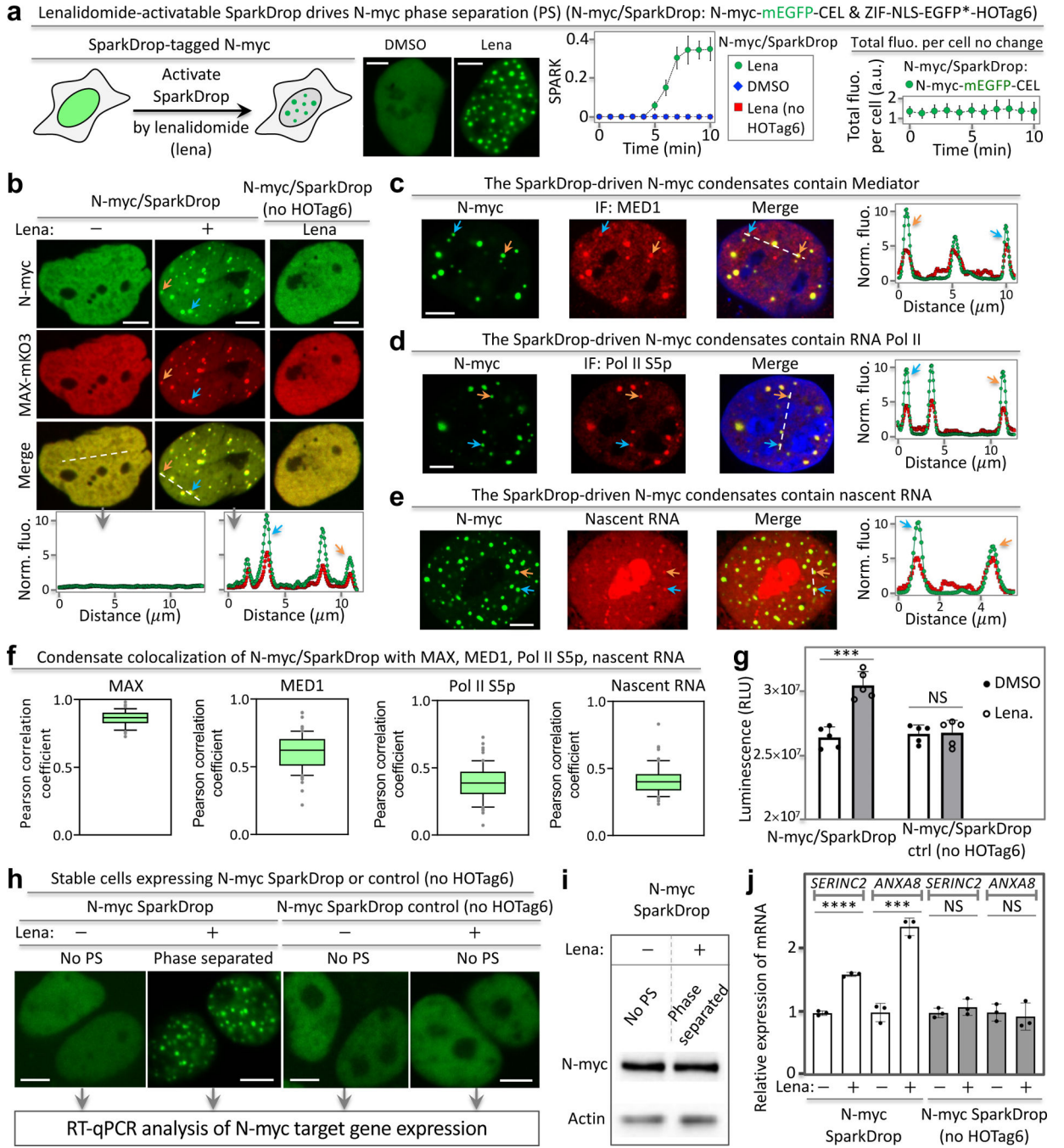


Fig. 6. Transcriptional role of N-myc phase separation revealed using the chemogenetic tool SparkDrop.

(a) SparkDrop drives N-myc phase separation without change of protein abundance. From left to right: schematic and representative images of N-myc/SparkDrop, SPARK value and total fluorescence change upon lenalidomide incubation. (b) Fluorescence images of N-myc/SparkDrop and a no-HOTag6 control with MAX-mKO3. The profile of fluorescence intensity corresponds to the position indicated by the dashed line. (c – e) Fluorescence images showing SparkDrop-driven N-myc condensates contain transcriptional machinery

components like MED1 (c), RNA Pol II S5p (d), and nascent RNA (e). The profile of fluorescence intensity corresponds to the position indicated by the dashed line. Arrows in the profile plot point to the condensates with colocalization. (f) Co-localization assessment by Pearson's correlation coefficient. Center lines show the median values. Green boxes contain the 25th to 75th percentiles of dataset. Black whiskers mark the 10th and 90th percentiles. Outliers are marked with grey dots. $N_{MAX} = 64$, $N_{MED1} = 67$, $N_{Pol\ II-S5P} = 68$, $N_{nascent\ RNA} = 64$ cells. (g) Quantitative analysis of SH-EP cell proliferation using CellTiter-Glo with N-myc in non-phase-separated vs phase-separated state. Luminescence was measured after the cells were treated with DMSO or lenalidomide (1 μ M) for 72 hrs. Data are mean \pm SD (n = 5). *P* value, two-sided non-paired t-test. (h) Confocal fluorescence images of cells stably expressing SparkDrop-tagged N-myc or the control. The cells were incubated with lenalidomide or DMSO for 16 hrs. RT-qPCR was then performed. PS: phase separation. (i) Western blot of N-myc from cells treated with and without lenalidomide. (j) RT-qPCR of N-myc-regulated genes SERINC2 and ANXA8 in cells without and with N-myc PS. Data are mean \pm SD (n = 3). *P* value, two-sided non-paired t-test. Scale bars: 5 μ m (a – e, h).

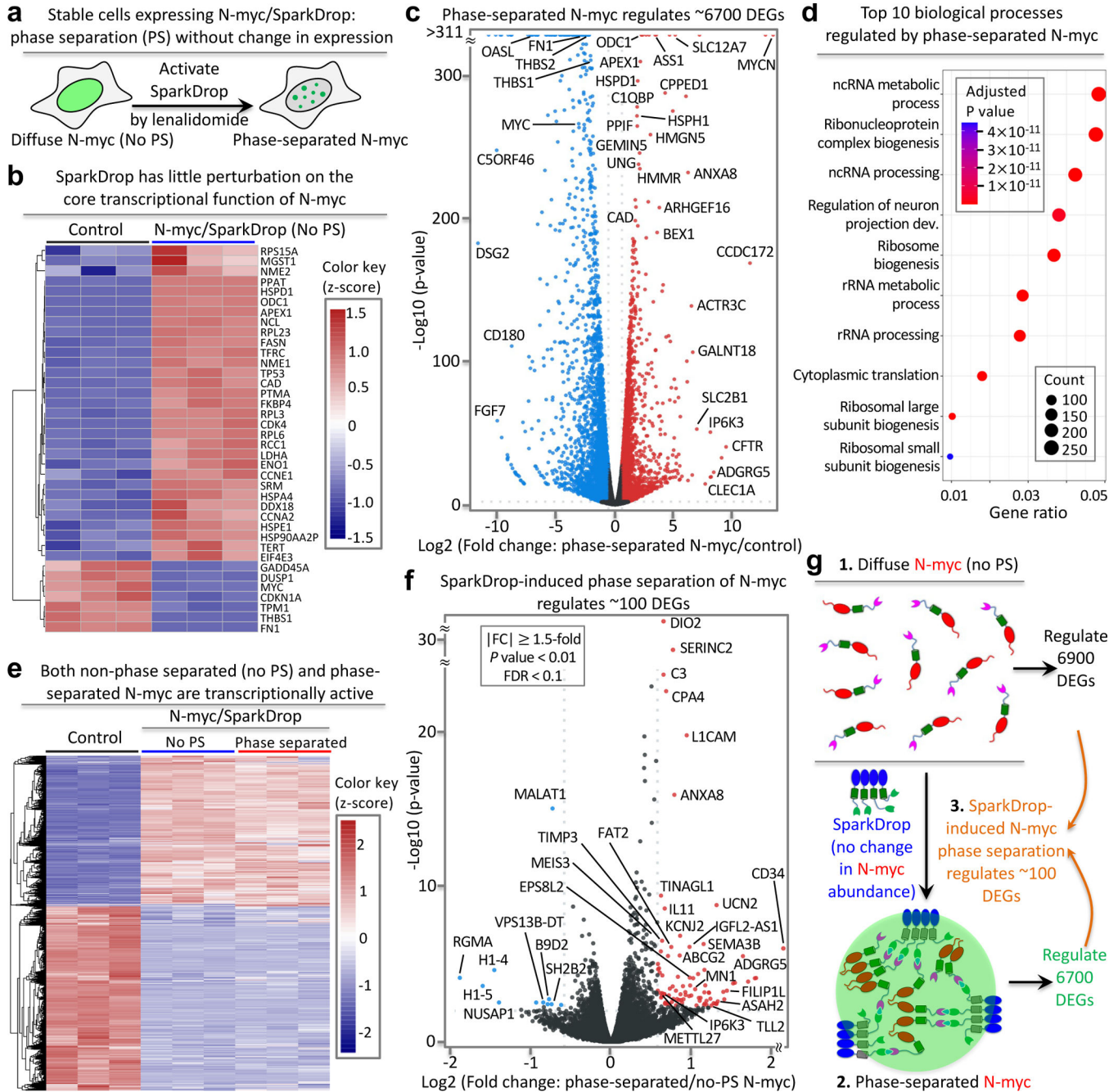


Fig. 7. SparkDrop-induced phase separation of N-myc regulates transcription of a small percentage of genes.

(a) Schematic of SparkDrop-based N-myc phase separation without change of protein abundance levels. (b) Heatmap of genes regulated in response to N-myc/SparkDrop-expression (without phase separation) showing expression levels of core target genes of N-myc. (c) Volcano plot showing DEGs that are regulated by phase-separated N-myc compared to no N-myc expression. The significantly up- and down-regulated mRNAs ($|FC| \geq 1.5$, $p\text{-value} < 0.01$, $FDR < 0.1$) are marked in red and blue, respectively. Black dots indicate no significant changes. P values and fold change came from DESeq2 with

default setting. **(d)** GO enrichment analysis of biological processes that are regulated by phase-separated N-myc. *P* value, double sided hypergeometric test. **(e)** Heat map showing DEGs regulated by diffuse N-myc (non-phase separated) and phase-separated N-myc. The color represents z-scores. SH-EP cells expressing N-myc/SparkDrop were treated with DMSO or lenalidomide for 16 hours, followed by processing for RNA-seq. **(f)** Volcano plot showing DEGs that are regulated by SparkDrop-induced phase separation of N-myc (i.e., phase-separated N-myc compared to non-phase separated N-myc). The mRNAs with significant up- and down-regulation ($|FC| \geq 1.5$, $p\text{-value} < 0.01$, $FDR < 0.1$) are marked in red and blue, respectively. Black dots represent mRNAs with no significant changes. *P* values and fold change came from DESeq2 with default setting. **(g)** Schematic showing transcriptional regulation by diffuse N-myc (no phase separation), phase separated-N-myc, as well as N-myc phase separation (induced by SparkDrop), i.e., the difference between them.